Matched Filtering-Based Channel Estimation for AFDM Systems in Doubly Selective Channels

Xiangjun Li, Zilong Liu, Zhengchun Zhou, and Pingzhi Fan

***Abstract*—Affine frequency division multiplexing (AFDM) has recently emerged as an excellent backward-compatible 6G waveform. In this paper, we study matched filtering (MF) assisted channel estimation (CE) for AFDM systems in complex doubly selective channels. By deriving the complete input-output relationship of the continuous-time signal, the inter-chirp-carrier interference, signal-to-interference-plus-noise ratio (SINR), and the effective SINR loss of AFDM, are investigated in discrete affine Fourier transform (DAFT) domain. Further, we propose two low-complexity methods for constructing the channel matrix by taking advantage of its inherent discrete Fourier transform structure and the staircase structure of the piecewise functions in the channel matrix, respectively. It is shown that complexity reduction by at least two orders of magnitude can be achieved for a large number of chirp subcarriers. For the CE problem in doubly selective channels, we introduce an MF assisted CE scheme. This allows us to sequentially estimate the parameters of each path by exploiting the separability and approximate orthogonality of different paths in the DAFT domain, thus leading to significantly reduced complexity. Furthermore, based on generalized Fibonacci search (GFS), an MF-GFS scheme is proposed to avoid significantly redundant computation, which can be extended to typical wide-band systems. Extensive simulation results indicate that the proposed schemes offer superior advantages in terms of their improved communication performance and lower complexity.**

***Index Terms*—Affine frequency division multiplexing (AFDM), channel estimation, doubly selective channels, matched filtering.**

I. Introduction

THE sixth generation (6G) communication systems are deemed to support ultra-reliable, low-latency, and high-rate communications in highly dynamic scenarios, such as vehicle-to-everything (V2X) systems, unmanned aerial vehicles, high-speed trains, and low-earth-orbit (LEO) satellites. Traditional orthogonal frequency-division multiplexing (OFDM) may be infeasible due to significant inter-carrier interference caused by high mobility [1]–[3].

Several waveforms that can adapt to high-mobility scenarios have been studied. Among many others, a representative waveform is orthogonal time-frequency space (OTFS) whose information symbols are transmitted in the delay-Doppler (DD) domain through two-dimensional (2D) orthogonal basis functions [4]–[6]. Since each information symbol in the DD domain spans the entire time-frequency grid, OTFS is able to achieve a significant improvement in error rate performance compared to OFDM [5]–[11]. In addition, Zak-OTFS [12], [13] has emerged as a strong competitor to conventional OTFS in recent years, offering an alternative Zak-transform-based formulation that preserves the DD domain advantages while enabling flexible waveform implementations. However, OTFS requires radical change for the transceiver design and hence may not permit a seamless integration into the legacy OFDM-based wireless systems.

Recently, affine frequency division multiplexing (AFDM) has emerged as an excellent backward-compatible 6G waveform for efficient and reliable high-mobility communications [14]–[21]. With minimum modification of OFDM, AFDM modulates the data symbols using multiple orthogonal chirp-carriers. The modulation is carried out through discrete affine Fourier transform (DAFT), enabling efficient mapping between the DAFT domain and the time domain. By appropriately tuning the chirp rate according to the Doppler profile of the channel, AFDM enables proper spreading in the time-frequency domain, thus allowing it to achieve the full diversity over doubly selective channels. Besides, the sparsity and compactness of the channel in the DAFT domain can be exploited for reducing the pilot overhead. Special cases of AFDM include DAFT-OFDM [22] and orthogonal chirp division multiplexing (OCDM) [23], yet they may not be able to achieve the full diversity [16].

A plethora of recent works have further explored AFDM. By flexibly selecting the chirp parameter, AFDM can achieve significant performance improvements in several aspects. Inspired by the index modulation (IM) for OFDM [24], IM-AFDM systems were studied in [25]–[29] for improving the spectral efficiency. From the PAPR reduction aspect, the chirp-permuted AFDM was employed in [29], while the grouped pre-chirp selection algorithm was proposed in [30].

The integration of generalized spatial modulation (GSM) and AFDM, called GSM-AFDM, was studied in [31] to design low-power and high-performance multiple-input and multiple-output (MIMO) systems. For 6G integrated sensing and communications (ISAC), several studies demonstrated the advantages of AFDM-empowered ISAC [32]–[35] systems. To support massive machine-type high-mobility communications, AFDM was also exploited as the building waveform for sparse code multiple access (SCMA) systems in [36].

Most existing works assume that the receiver has perfect channel information to achieve excellent transmission performance. In practice, however, channel estimation (CE) is generally required for coherent receiving systems. Similar to

Xiangjun Li, Zhengchun Zhou and Pingzhi Fan are with the School of Info Sci & Tech, Southwest Jiaotong University, Chengdu, China. Zilong Liu is with the School of Computer Science and Electronics Engineering, University of Essex, U. K. Corresponding author: Zhengchun Zhou. Emails: lxj@my.swjtu.edu.cn; zilong.liu@essex.ac.uk; zzc@swjtu.edu.cn; pzfan@swjtu.edu.cn.

the traditional CE scheme in OTFS [8], the least squares (LS) estimator was investigated in [37] along with a reasonable threshold to estimate the path parameters. By exploiting the sparsity of the channel, the authors in [38]–[40] modeled CE as a sparse signal recovery problem and estimated the channel using the compressed sensing (CS) algorithm.

The aforementioned schemes mostly assume that the normalized delay and Doppler values of the paths are integers. Nevertheless, the real-life channel response of each path typically does not align with the grid point in the DAFT domain. That is, the normalized delay and Doppler values may have fractional components, potentially resulting in a loss of channel sparsity, as well as degradation of CE performance in the DAFT domain. To address this issue, a CE scheme for MIMO-AFDM based on the diagonal reconstruction of the subchannel matrix was proposed in [41]. Their scheme directly estimates the effective channel matrix instead of the specific channel parameters. An approximate maximum likelihood CE scheme for AFDM was proposed in [16] by assuming that the delay of each propagation path is different and the number of paths is known *a priori*. In addition, the joint estimation of all paths in [16] results in high computational complexity.

Based on the correlation between AFDM basis functions and the received signal, this work investigates matched filtering (MF) assisted CE in doubly selective channels for AFDM systems. We differentiate integer-delay-fractional-Doppler (IDFD) and fractional-delay-fractional-Doppler (FDFD) channels and develop advanced MF-CE schemes. The main contributions are summarized as follows:

- Firstly, we adopt the input-output (I/O) relationship in the time domain, in alignment with that employed in existing OTFS-related research. We derive the corresponding I/O relationship for continuous-time signals and then present a comprehensive analysis on the inter-chirp-carrier-interference (ICCI), signal-to-interference-plus-noise ratio (SINR), and effective SINR loss.
- Secondly, for FDFD channels, we propose two low-complexity methods for fast channel matrix construction. The first method exploits the inherent DFT structure of the channel matrix, enabling efficient computation via fast Fourier transform (FFT). The second method leverages the staircase structure of the piecewise functions in the channel matrix to directly calculate partial sums. For large numbers of subcarriers, the proposed methods can reduce the complexity by at least two orders of magnitude.
- Thirdly, for FDFD channels, we propose an MF CE scheme with joint DD estimation (MF-JE). By leveraging the separability and orthogonality of different paths, our proposed MF scheme is able to eliminate the matrix inversion operation, decouple multipath estimation, and narrow the search range, thus leading to significantly reduced complexity. In addition, by decoupling the DD estimation to further narrow the search region, a more efficient MF (MF-DE) CE scheme is developed at the cost of a slight performance loss.
- Fourthly, based on the generalized Fibonacci search (GFS) algorithm[1] [42]–[44], we propose an MF-GFS-DE CE scheme for FDFD channels. It is found that our proposed scheme can reduce the amount of search when estimating fractional parameters, yielding a significant reduction in redundant computations whilst outperforming the proposed MF scheme.
- Finally, we extend the proposed MF CE to the IDFD channels in typical wide-band systems (i.e., millimeter-wave communication systems) whereby the bandwidth is sufficiently large to approximate the normalized delay shifts to be integers. Given that the objective function for estimating fractional Doppler can also be demonstrated to be unimodal, an MF-GFS scheme is proposed for IDFD channels. Simulation results indicate that the proposed schemes offer advantages in both computational complexity and performance.

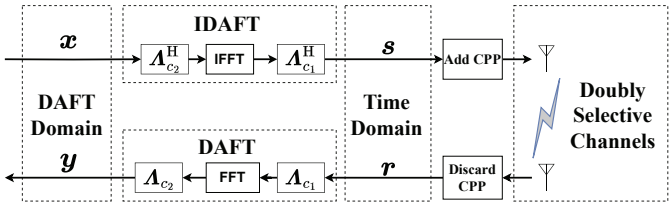

Fig. 1: AFDM system block diagram.

The rest of this paper is organized as follows. Section II reviews the basic concepts of AFDM. Section III analyzes channel in the DAFT domain. Section IV introduces the MF CE scheme and MF-GFS CE scheme. Section V gives the simulation results. Finally, Section VI concludes this paper.

Notations: The m-th element of vector $\boldsymbol{x}$ is denoted by $x[m]$, the element in the m-th row and n-th column of matrix $\boldsymbol{X}$ is $X[m,n]$. $(\cdot)^*$, $(\cdot)^{\mathrm{T}}$ and $(\cdot)^{\mathrm{H}}$ denote the conjugate, transpose, and Hermitian operations, respectively. $\mathrm{diag}(\cdot)$ is to convert a vector into a diagonal matrix or extract the diagonal elements of a matrix. $\lceil\cdot\rceil$, $\lfloor\cdot\rfloor$, and $\lfloor\cdot\rceil$ denote the ceiling, floor, and nearest-integer operators, respectively. $E\{\cdot\}$ is the expected operation. $\{\boldsymbol{x}\times\boldsymbol{y}\}$ is the Cartesian product. $\delta(\cdot)$ is the Dirac delta function. $\boldsymbol{I}_N$ is the $N\times N$ identity matrix. $|\cdot|$ denotes the modulus operation. $[\cdot]_N$ is the mod-N operation.

II. System Models

A. AFDM modulation

Assume that the number of chirp subcarriers is N, the subcarrier spacing is Δf (Hz), the bandwidth is $B=N\Delta f$, and the duration of an AFDM symbol is T. The DAFT domain axis is sampled at multiple times of Δf to obtain a discrete grid, i.e., $\boldsymbol{\Xi}=\{n\Delta f, n=0,\cdots,N-1\}$. In this paper, the AFDM system is illustrated in Fig. 1. For the transmitter (TX) side, consider a set of N information symbols $\{x[n], n=0,\cdots,N-1\}$ from a modulation alphabet $\mathbb{A}$ of size M_{mod} (e.g. QAM symbols), which are arranged on the

[1]GFS is an unconstrained nonlinear optimization method for unimodal functions. The ratio of two consecutive generalized Fibonacci numbers (GFNs) approximates the golden ratio. In GFS, two consecutive GFNs are used to non-uniformly divide the search interval, thereby efficiently narrowing the search range, reducing complexity, and enabling more accurate estimation.

DAFT domain grid $\boldsymbol{\Xi}$. The AFDM modulator first employs inverse DAFT (IDAFT) to map $x[n]$ to $s[\bar{n}]$, as shown below:

$$s[\bar{n}] = \sum_{n=0}^{N-1} x[n]\phi_n[\bar{n}], \tag{1}$$

where $\phi_n[\bar{n}] = \frac{1}{\sqrt{N}} e^{j2\pi\left(c_1\bar{n}^2 + c_2 n^2 + \frac{\bar{n}n}{N}\right)}$, $\bar{n} \in \{0, \cdots, N-1\}$ is the time index, $n \in \{0, \cdots, N-1\}$ is the chirp subcarrier index in the DAFT domain, c_1 and c_2 are DAFT parameters. Note that with a proper c_1, the paths are separable in the DAFT domain, enabling AFDM to achieve full diversity in doubly selective channels, i.e., [16]

$$c_1 = \frac{2(k_{\max} + \xi) + 1}{2N}, \tag{2}$$

where ξ is a small non-negative integer introduced to suppress fractional Doppler. This paper sets c_1 to the value in (2) by default. Other values of c_1 may be possible as long as AFDM achieves full diversity. (1) can be rewritten as

$$\boldsymbol{s} = \boldsymbol{A}^{\mathrm{H}}\boldsymbol{x}, \tag{3}$$

where $\boldsymbol{x} = [x[0], \cdots, x[N-1]]^{\mathrm{T}} \in \mathbb{C}^{N\times 1}$, $\boldsymbol{s} = [s[0], \cdots, s[N-1]]^{\mathrm{T}} \in \mathbb{C}^{N\times 1}$, $\boldsymbol{A} = \boldsymbol{\Lambda}_{c_2}\boldsymbol{F}\boldsymbol{\Lambda}_{c_1}$ is the normalized DAFT matrix, $\boldsymbol{F}$ is the normalized DFT matrix, $\boldsymbol{\Lambda}_c = \mathrm{diag}(e^{-j2\pi c n^2}, n = 0, 1, ..., N-1)$. Before transmission, a chirp-periodic prefix (CPP) [16] of length L_{CPP} is also employed. To reflect the spectral wrapping inherent in the AFDM signal, the continuous transmit signal in $0 \leqslant t < T$ should be expressed as [21]

$$s(t) = \frac{1}{\sqrt{N}} \sum_{n=0}^{N-1} x[n]\, g_{\mathrm{tx}}(t)\, \phi_n(t), \tag{4}$$

where $g_{\mathrm{tx}}(t)$ is the transmit pulse-shaping filter, $\phi_n(t) = e^{j2\pi\left(c_2 n^2 + \frac{c_1}{T_s^2}t^2 + \frac{n}{T}t + \varphi_n(t)\right)}$, $T_s = \frac{T}{N}$ is the sampling period, $\varphi_n(t) = \sum_{q=0}^{2Nc_1} \alpha_{n,q}(t)$, $q \in \{0, 1, \cdots, 2Nc_1\}$, $\alpha_{n,q}(t)$ is given by

$$\alpha_{n,q}(t) = \begin{cases} \lfloor \frac{q\left(q - \frac{n}{N}\right)}{2c_1} \rfloor - \frac{q}{T_s}t, & t_{n,q} \leq t < t_{n,q+1} \\ 0, & \text{otherwise} \end{cases}, \tag{5}$$

$$t_{n,q} = \begin{cases} 0, & q = 0 \\ \frac{qN-n}{2Nc_1}T_s, & 1 \leq q \leq 2Nc_1 \end{cases}. \tag{6}$$

B. Doubly Selective Channels

Considering the sparsity of the channel, the channel response $h(\tau, \nu)$ can be expressed as

$$h(\tau, \nu) = \sum_{i=1}^{P} h_i \delta(\nu - \nu_i)\, \delta(\tau - \tau_i), \tag{7}$$

where h_i, $\tau_i \in [0, \tau_{\max}]$ and $\nu_i \in [-\nu_{\max}, \nu_{\max}]$ are the channel gain, delay and Doppler parameters of the i-th path, respectively, P is the number of paths. $\nu_{\max}$ and $\tau_{\max}$ are the maximum Doppler and delay, respectively. The normalized delay l_{τ_i} and Doppler k_{ν_i} satisfy

$$\tau_i = \frac{l_{\tau_i}}{N\Delta f},\ \nu_i = k_{\nu_i}\Delta f, \tag{8}$$

where $k_{\nu_i} = \bar{k}_{\nu_i} + \kappa_{\nu_i} \in [-k_{\max}, k_{\max}]$, $l_{\tau_i} = \bar{l}_{\tau_i} + \iota_{\tau_i} \in [0, l_{\max}]$, $\bar{k}_{\nu_i}$ and $\bar{l}_{\tau_i}$ are both integer parts, $\kappa_{\nu_i} \in [-0.5, 0.5]$ and $\iota_{\tau_i} \in [-0.5, 0.5]$ are both fractional parts, $k_{\max} = \lceil \frac{N\nu_{\max}}{B} \rceil$, $l_{\max} = \lceil \tau_{\max} B \rceil$. Due to the finite B and T, there is generally fractional delay and Doppler. $\nu_{\max}$ and $\tau_{\max}$ can usually be considered known a priori [9]. However, the number of scatterers in the environment is usually unpredictable, resulting in the uncertainty of P.

After digital-to-analog conversion, the transmitted signal is represented by $s(t)$. In [16], the received signal $r(t)$ is

$$r(t) = \iint h(\tau, \nu) s(t - \tau) e^{j2\pi\nu t} \mathrm{d}\tau \mathrm{d}\nu + \tilde{w}(t). \tag{9}$$

However, to be consistent with existing OTFS-related research, $r(t)$ in this paper is given by [4]

$$r(t) = \iint h(\tau, \nu) s(t - \tau) e^{j2\pi\nu(t-\tau)} \mathrm{d}\tau \mathrm{d}\nu + \tilde{w}(t), \tag{10}$$

where $\tilde{w}(t)$ is the additive white Gaussian noise. The two interpretations of the channel impulse response differ by a term $e^{-j2\pi\nu\tau}$. As long as the notation is consistent, equivalent results can be obtained by using either definition.

After discarding CPP, $r(t)$ is given by

$$r(t) = \sum_{i=1}^{P} h_i s(t - \tau_i) e^{j2\pi\nu_i(t-\tau_i)} + \tilde{w}(\bar{n}), \tag{11}$$

where $\tilde{w}(\bar{n})$ is a zero-mean Gaussian noise with variance σ^2.

C. AFDM Demodulation

At the receiver side, demodulation is performed to obtain $y[m]$ in the DAFT domain, i.e.,

$$y[m] = \sum_{\bar{n}=0}^{N-1} \left(r(t)\, g_{\mathrm{rx}}(t)\, \phi_m^*(t) \right)|_{t=\bar{n}T_S}, \tag{12}$$

where $g_{\mathrm{rx}}(t)$ is the receive pulse-shaping filter. For simplicity, this paper adopts rectangular pulse shaping.

III. Channel Analysis in The DAFT Domain

This section analyzes the I/O relationship, ICCI, SINR, and the effective SINR loss. It also presents two low-complexity methods for channel matrix construction.

A. I/O Relation of AFDM

Theorem 1. The $y[m]$ can be expressed as

$$y[m] = \sum_{n=0}^{N-1} x[n]\, H_{\mathrm{eff}}[m, n] + w[n], \tag{13}$$

$$H_{\mathrm{eff}}[m, n] = \sum_{i=1}^{P} h_i \mathcal{G}(m, n, k_{\nu_i}, l_{\tau_i}), \tag{14}$$

$$\mathcal{G}(m, n, k_{\nu_i}, l_{\tau_i}) = \alpha(m, n, k_{\nu_i}, l_{\tau_i}) \mathcal{F}(m, n, k_{\nu_i}, l_{\tau_i}), \tag{15}$$

$$\alpha(m, n, k_{\nu_i}, l_{\tau_i}) = e^{\frac{-j2\pi}{N}\left(-Nc_1 l_{\tau_i}^2 + \left(n + k_{\nu_i}\right) l_{\tau_i} + Nc_2\left(m^2 - n^2\right)\right)}, \tag{16}$$

$$
\begin{aligned}
&\mathcal{F}\left(m,n,l_{\tau_i},k_{\nu_i}\right)\\
&=\frac{1}{N}\sum_{\bar{n}=0}^{N-1}e^{\frac{-j2\pi}{N}\left(\left(m-n+2Nc_1l_{\tau_i}-k_{\nu_i}\right)\bar{n}-Nd_{\bar{n},n}\iota_{\tau_i}\right)}\\
&=\begin{cases}
\frac{1}{N}\delta\left(\left[m-n+2Nc_1l_{\tau_i}-k_{\nu_i}\right]_N\right) & \kappa_{\nu_i}=0,\iota_{\tau_i}=0\\
\frac{1}{N}\frac{e^{-j2\pi\left(m-n+2Nc_1l_{\tau_i}-k_{\nu_i}\right)}-1}{e^{\frac{-j2\pi}{N}\left(m-n+2Nc_1l_{\tau_i}-k_{\nu_i}\right)}-1} & \kappa_{\nu_i}\neq 0,\iota_{\tau_i}=0\\
\frac{1}{N}\sum_{\bar{n}=0}^{N-1}e^{j2\pi d_{\bar{n},n}\iota_{\tau_i}} & \kappa_{\nu_i}\neq 0,\iota_{\tau_i}\neq 0\\
\quad\times e^{\frac{-j2\pi}{N}\left(m-n+2Nc_1l_{\tau_i}-k_{\nu_i}\right)\bar{n}} &
\end{cases}.
\end{aligned}
\tag{17}
$$

Proof: The proof is given in Appendix A. ∎

$\mathcal{G}(m,n,k_{\nu_i},l_{\tau_i})$ is the AFDM basis function used for subsequent CE. Rewriting (13) into another matrix form, we have

$$
\boldsymbol{y}=\boldsymbol{H}_{\text{eff}}\boldsymbol{x}+\boldsymbol{w},
\tag{18}
$$

where the effective channel matrix $\boldsymbol{H}_{\text{eff}}$ is the matrix form of $H_{\text{eff}}\left(m,n\right)$ in the DAFT domain. In addition, the permutation matrix can typically model the integer delay in the time-domain channel matrix $\boldsymbol{H}_{\text{T}}$. However, this method fails for fractional delay. Since $\boldsymbol{H}_{\text{eff}}=\boldsymbol{A}\boldsymbol{H}_{\text{T}}\boldsymbol{A}^{\text{H}}$, $\boldsymbol{H}_{\text{T}}$ is given by $\boldsymbol{H}_{\text{T}}=\boldsymbol{A}^{\text{H}}\boldsymbol{H}_{\text{eff}}\boldsymbol{A}$.

B. Analysis of ICCI and the Channel in the DAFT Domain

Since $\alpha\left(m,n,k_{\nu_i},l_{\tau_i}\right)$ is a phase factor, the characteristics of $\boldsymbol{H}_{\text{eff}}$ are determined by $\mathcal{F}\left(m,n,l_{\tau_i},k_{\nu_i}\right)$.

1) Integer-delay-integer-Doppler (IDID) Channels: In this case, $l_{\tau_i}=\bar{l}_{\tau_i}$, $k_{\nu_i}=\bar{k}_{\nu_i}$. Since $\mathcal{F}\left(m,n,l_{\tau_i},k_{\nu_i}\right)$ simplifies to $\frac{1}{N}\delta\left(\left[m-n+2Nc_1l_{\tau_i}-k_{\nu_i}\right]_N\right)$, (13) will be simplified to

$$
y\left[m\right]=\sum_{i=1}^{P}h_i\alpha(m,n,k_{\nu_i},l_{\tau_i})x\left[n\right]+w\left[n\right],
\tag{19}
$$

where $n=\left[m+2Nc_1l_{\tau_i}-k_{\nu_i}\right]_N$. For the i-th path, since only the transmitted signal $x\left[\left[m+2Nc_1l_{\tau_i}-k_{\nu_i}\right]_N\right]$ constitutes $y\left[m\right]$, there is no ICCI for the IDID channels.

2) IDFD Channels: In this case, $l_{\tau_i}=\bar{l}_{\tau_i}$, $k_{\nu_i}=\bar{k}_{\nu_i}+\kappa_{\nu_i}$. Since $\iota_{\tau_i}=0$, we have

$$
\begin{aligned}
\mathcal{F}\left(m,n,l_{\tau_i},k_{\nu_i}\right)&=\frac{e^{-j2\pi\beta}-1}{Ne^{\frac{-j2\pi}{N}\beta}-1}\\
&=\frac{1}{N}e^{-j(N-1)\pi\frac{\beta}{N}}\frac{\sin\left(\pi\beta\right)}{\sin\left(\frac{\pi\beta}{N}\right)},
\end{aligned}
\tag{20}
$$

where $\beta=m-n+2Nc_1l_{\tau_i}-k_{\nu_i}$. Due to the existence of fractional Doppler κ_{ν_i}, $\mathcal{F}(m,n,k_{\nu_i},l_{\tau_i})$ will not be zero for a given m and any n. Some works [6], [16] have shown that $|\mathcal{F}(m,n,k_{\nu_i},l_{\tau_i})|$ has a peak at $n=\left[m+2Nc_1l_{\tau_i}-\bar{k}_{\nu_i}\right]_N$ and decreases significantly as n moves away from $\left[m+2Nc_1l_{\tau_i}-\bar{k}_{\nu_i}\right]_N$. Therefore, we only need to consider the $2\xi+1$ principal values of $\mathcal{F}(m,n,k_{\nu_i},l_{\tau_i})$ around the peak of $\left[m+2Nc_1l_{\tau_i}-\bar{k}_{\nu_i}\right]_N$, i.e., $\left[m+2Nc_1l_{\tau_i}-\bar{k}_{\nu_i}-\xi\right]_N\leqslant n\leqslant\left[m+2Nc_1l_{\tau_i}-\bar{k}_{\nu_i}+\xi\right]_N$. Based on this good approximation, we can re-express $y\left[m\right]$ in (13) as

$$
\begin{aligned}
y\left[m\right]&\approx\sum_{i=1}^{P}\sum_{n=\left[m+2Nc_1l_{\tau_i}-\bar{k}_{\nu_i}-\xi\right]_N}^{\left[m+2Nc_1l_{\tau_i}-\bar{k}_{\nu_i}+\xi\right]_N}x\left[n\right]h_i\mathcal{G}(m,n,k_{\nu_i},l_{\tau_i})\\
&\approx\sum_{i=1}^{P}\sum_{q=-\xi}^{\xi}x\left[n_q\right]h_i\alpha(m,n_q,k_{\nu_i},l_{\tau_i})\\
&\quad\times\frac{e^{-j2\pi(q-\kappa_{\nu_i})}-1}{Ne^{-j\frac{2\pi}{N}(q-\kappa_{\nu_i})}-N},
\end{aligned}
\tag{21}
$$

where $n_q=\left[m-q+2Nc_1l_{\tau_i}-\bar{k}_{\nu_i}\right]_N$. From (21), it is evident that $y\left[m\right]$ is approximately a linear combination of $P\left(2\xi+1\right)$ transmitted signals. For the $2\xi+1$ transmitted signals in the i-th path, only $x\left[n_{q|q=0}\right]$ is the main source of $y\left[m\right]$, and the other 2ξ signals can be regarded as interference. This interference is caused by the chirp-subcarriers near the $n_{q|q=0}$-th chirp-subcarrier, so it is called ICCI.

3) FDFD Channels: In this case, $l_{\tau_i}=\bar{l}_{\tau_i}+\iota_{\tau_i}$, $k_{\nu_i}=\bar{k}_{\nu_i}+\kappa_{\nu_i}$. Since $\iota_{\tau_i}\neq 0$, we have

$$
\mathcal{F}\left(m,n,k_{\nu_i},l_{\tau_i}\right)=\frac{1}{N}\sum_{\bar{n}=0}^{N-1}e^{\frac{-j2\pi}{N}\eta_{m,n}^{(i)}\bar{n}}e^{j2\pi(d_{\bar{n},n}-2\bar{n}c_1)\iota_{\tau_i}},
\tag{22}
$$

where $\eta_{m,n}^{(i)}=m-n-\chi_i-\kappa_{\nu_i}$, $\chi_i=-2Nc_1\bar{l}_{\tau_i}+\bar{k}_{\nu_i}$ is the equivalent shift of the i-th path. Since $\left(d_{\bar{n},n}-2\bar{n}c_1\right)\iota_{\tau_i}$ is small, it does not affect the peak position. For the i-th path, the condition for the occurrence of the main peak of $|\mathcal{F}\left(m,n,k_{\nu_i},l_{\tau_i}\right)|$ is

$$
m=m_{\text{m-peak}}^{(i)}=\left[n+\chi_i\right]_N.
\tag{23}
$$

In addition, $|\mathcal{F}\left(m,n,k_{\nu_i},l_{\tau_i}\right)|$ displays some high-level local peaks. The positions of these local peaks are

$$
m_{\text{l-peak}}^{(i)}=m_{\text{m-peak}}^{(i)}\pm 2gNc_1,
\tag{24}
$$

where g is a small positive integer. In addition, as $m_{\text{l-peak}}^{(i)}$ moves away from $m_{\text{m-peak}}^{(i)}$, its local peaks decrease in magnitude. Therefore, for FDFD channels, these local peaks will lead to more severe ICCI. Simultaneously, local peaks in all paths further exacerbate the inter-path interference.

Based on the above analysis, since $|\mathcal{F}\left(m,n,k_{\nu_i},l_{\tau_i}\right)|$ contains non-negligible local peaks, the I/O relationship cannot be approximated and can only be expressed as (13). In addition, $N-1$ transmitted signals will generate ICCI for $y\left[m\right]$.

C. Low-Complexity Channel Matrix Construction

The rapid and low-complexity construction of channel matrices enables efficient system simulations, reduces computational overhead, and facilitates real-time signal processing, which is particularly important for high-dimensional or large-scale systems.

The complexity of constructing $\boldsymbol{H}_{\text{eff}}$ mainly comes from the construction of the $\mathcal{F}\left(m,n,l_{\tau_i},k_{\nu_i}\right)$. For both IDID and IDFD channels, $\mathcal{F}\left(m,n,l_{\tau_i},k_{\nu_i}\right)$ can be converted into the simple form of the summation-free version in (17). However, for FDFD channels, due to the presence of $d_{\bar{n},n}\iota_{\tau_i}$,

$\mathcal{F}(m,n,l_{\tau_i},k_{\nu_i})$ cannot be further simplified. Using the element-wise summation (ES) method to construct the channel matrix leads to high complexity, especially for large N.

1) The FFT-based Method:

We rewrite $\mathcal{F}(m,n,l_{\tau_i},k_{\nu_i})$ as

$$\begin{aligned}\mathcal{F}(m,n,l_{\tau_i},k_{\nu_i}) &= \sum_{\bar{n}=0}^{N-1} e^{\frac{-j2\pi}{N}\left(\left(2Nc_1 l_{\tau_i}-k_{\nu_i}-n\right)\bar{n}-Nd_{\bar{n},n}\iota_{\tau_i}\right)} \\ &\quad\times e^{\frac{-j2\pi}{N}m\bar{n}} \\ &= \sum_{\bar{n}=0}^{N-1} u(\bar{n},n)\, e^{\frac{-j2\pi}{N}m\bar{n}},\end{aligned} \tag{25}$$

where $u(\bar{n},n) = e^{\frac{-j2\pi}{N}\left(\left(2Nc_1 l_{\tau_i}-k_{\nu_i}-n\right)\bar{n}-Nd_{\bar{n},n}\iota_{\tau_i}\right)}$. This is exactly the DFT Transform. Utilizing the FFT enables the rapid construction of $\mathcal{F}(m,n,l_{\tau_i},k_{\nu_i})$.

2) The Segment-wise Summation (SS) Method:

Considering the special structure of $d_{\bar{n},n}$, $|\mathcal{F}(m,n,k_{\nu_i},l_{\tau_i})|$ can be simplified into a relatively simple segment-wise summation form. $d_{\bar{n},n}$ exhibits a staircase structure. For a given fixed n, the staircase has R_n levels. In addition, let the starting index, width, and value of each level are $\bar{n}_{r,n}$, $L_{r,n}$, and $d_{r,n}$, respectively. Therefore, (22) can be rewritten as

$$\begin{aligned}\mathcal{F}(m,n,l_{\tau_i},k_{\nu_i}) &= \frac{1}{N}\sum_{r=0}^{R_n-1} e^{j2\pi d_{r,n}\iota_{\tau_i}} \sum_{\bar{n}=\bar{n}_{r,n}}^{\bar{n}_{r,n}+L_{r,n}-1} e^{\frac{-j2\pi}{N}\beta\bar{n}} \\ &= \frac{1}{N\sin\left(\frac{\pi\beta}{N}\right)}\sum_{r=0}^{R_n-1}\sin\left(\frac{\pi}{N}\beta L_{r,n}\right)e^{j\varphi_{r,n}},\end{aligned} \tag{26}$$

where $\varphi_{r,n} = 2\pi d_{r,n}\iota_{\tau_i} - \frac{2\pi\beta}{N}\bar{n}^{\mathrm{c}}_{r,n}$, $\bar{n}^{\mathrm{c}}_{r,n} = \bar{n}_{r,n} + \frac{L_{r,n}-1}{2}$ is the central index of the r-th segment, $\beta = m-n+2Nc_1 l_{\tau_i} - k_{\nu_i}$. In addition, the mean R of R_n is generally $R \approx 2Nc_1$.

The ES method directly calculates each matrix element through explicit summation over all $\bar{n}$, resulting in a cubic complexity of $\mathcal{O}\left(N^3\right)$. The FFT-based method exploits the inherent DFT structure of the summation over $\bar{n}$ in $\mathcal{F}(m,n,l_{\tau_i},k_{\nu_i})$. By applying FFT to accelerate the computation, the overall complexity is reduced to $\mathcal{O}\left(N^2\log N\right)$. By leveraging the staircase structure of $d_{\bar{n},n}$, the SS method decomposes the summation over n into a series of closed expressions from each segment. Thus, the SS method effectively reduces the summation size from N to R, yielding complexity $\mathcal{O}\left(N^2R\right)$, far below the complexity of ES method.

D. SINR

For the receiver, linear minimum mean square error (LMMSE) equalization is used for $\boldsymbol{y}$ to mitigate the effects of noise and interference, i.e., $\hat{\boldsymbol{x}} = \boldsymbol{W}\boldsymbol{y}$, where $\hat{\boldsymbol{x}}$ is the estimate of $\boldsymbol{x}$, $\boldsymbol{W} = \left(\boldsymbol{H}_{\mathrm{eff}}^{\mathrm{H}}\boldsymbol{H}_{\mathrm{eff}} + \sigma^2\boldsymbol{I}_N\right)^{-1}\boldsymbol{H}_{\mathrm{eff}}^{\mathrm{H}}$. The signal of the n-th chirp-subcarrier is

$$\hat{x}[n] = T[n,n]\,x[n] + \sum_{m=0,m\neq n}^{N} T[n,m]\,x[m] + \tilde{w}[n], \tag{27}$$

where $n \in \{0,1,\cdots,N-1\}$, $\boldsymbol{T} = \boldsymbol{W}\boldsymbol{H}_{\mathrm{eff}}$. Therefore, the SINR on the n-th chirp-subcarrier is expressed as

$$\mathrm{SINR}_n = \frac{|T[n,n]|^2}{\sum_{m=0,m\neq n}^{N-1}|T[n,m]|^2 + \sigma^2\left\|\{\boldsymbol{W}\}_{n,:}\right\|^2}, \tag{28}$$

where $\{\cdot\}_{n,:}$ is the n-th row of the matrix.

E. Effective SINR Loss

For the IDID channels, according to the I/O relationship of (19), the corresponding peak power of the i-th path is

$$P_{\mathrm{IDD}} = |h_i|^2. \tag{29}$$

It can be seen that there is no SINR loss in this case.

For IDFD channels, based on subsection III-B-2), we have

$$|\mathcal{G}(m,n,k_{\nu_i},l_{\tau_i})| \leqslant \left|\frac{\sin(\pi\kappa_{\nu_i})}{N\sin\left(\frac{\pi\kappa_{\nu_i}}{N}\right)}\right|. \tag{30}$$

Therefore, the corresponding peak power of the i-th path is

$$P_{\mathrm{IDFD}} = |h_i|^2\left|\frac{\sin(\pi\kappa_{\nu_i})}{N\sin\left(\frac{\pi\kappa_{\nu_i}}{N}\right)}\right|^2. \tag{31}$$

Compared with (29), the SINR loss in the IDFD channels is

$$L_{\mathrm{SINR}}^{\mathrm{IDFD}} = 20\log_{10}\left|\frac{\sin(\pi\kappa_{\nu_i})}{N\sin\left(\frac{\pi\kappa_{\nu_i}}{N}\right)}\right|^2 \approx 20\log_{10}\left|\frac{\sin(\pi\kappa_{\nu_i})}{\pi\kappa_{\nu_i}}\right|^2, \tag{32}$$

where $\pi\kappa_{\nu_i}/N$ approaches zero, resulting in $\sin(\pi\kappa_{\nu_i}/N) \approx \pi\kappa_{\nu_i}/N$. In general, $N \gg \pi k_{\nu_i}$ is satisfied, therefore this approximation holds. Moreover, according to (32), increasing N cannot effectively reduce the SINR loss.

For FDFD channels, based on (22)-(23), the peak value $\mathcal{F}_{\max}$ of $|\mathcal{F}(m,n,k_{\nu_i},l_{\tau_i})|$ can be approximated as

$$\mathcal{F}_{\max} \approx \left|\frac{1}{N}\sum_{\bar{n}=0}^{N-1} e^{\frac{-j2\pi}{N}\eta^{(i)}_{m^{(i)}_{\mathrm{m-peak}},n}\bar{n}}\right| \approx \left|\frac{\sin(\pi\kappa_{\nu_i})}{\pi\kappa_{\nu_i}}\right|. \tag{33}$$

Therefore, increasing N does not reduce the SINR loss in the FDFD channel. The SINR loss in the FDFD channels is

$$L_{\mathrm{SINR}}^{\mathrm{FDFD}} = 20\log_{10}\left|\mathcal{F}\left(m^{(i)}_{\mathrm{m-peak}},n,k_{\nu_i},l_{\tau_i}\right)\right|^2. \tag{34}$$

Based on (34), Fig. 2 shows the effective SINR loss for different fractional delays and fractional Dopplers at $N = 64$. Increasing ι_{τ_i} or κ_{ν_i} results in more severe SINR loss. The maximum SINR loss is about 11.788 dB. Moreover, according to (32) and (33), increasing N cannot effectively reduce the SINR loss.

IV. MF and MF-GFS CE Schemes

In this section, we propose two low-complexity methods for estimating path parameters, by sequentially estimating the parameters of each individual path. Note that the chirp characteristic for separating different paths by c_1 is leveraged in the proposed CE schemes. Due to the fact that the chirp characteristic is invalidated by $c_1 = 0$ in OFDM systems, the proposed method cannot be directly applied to OFDM systems.

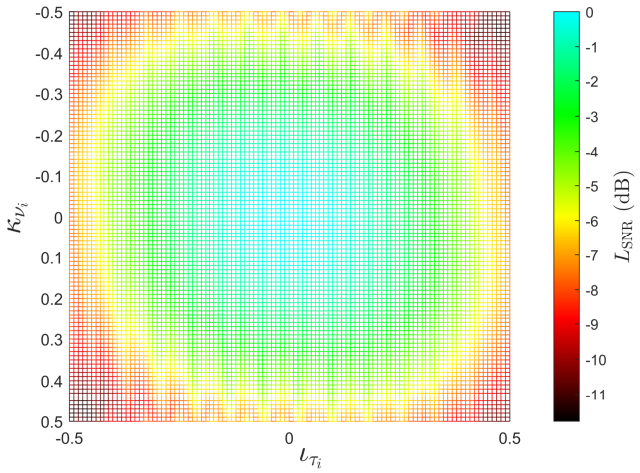

Fig. 2: Planform of SINR loss.

A. Problem Description

According to (13)-(17), the system model is

$$\boldsymbol{y} = \boldsymbol{A}\left(\boldsymbol{l}_\tau, \boldsymbol{k}_\nu\right)\boldsymbol{h} + \boldsymbol{w}, \tag{35}$$

where $\boldsymbol{y} \in \mathbb{C}^{N\times 1}$ and $\boldsymbol{w} \sim \mathcal{CN}\left(0, \sigma^2 \boldsymbol{I}_N\right) \in \mathbb{C}^{N\times 1}$ are vector forms of $y\left(m\right)$ and $w\left(m\right)$ respectively, vectors $\boldsymbol{l}_\tau = \left[l_{\tau_1}, \cdots, l_{\tau_P}\right]^{\mathrm{T}} \in \mathbb{R}^{P\times 1}$, $\boldsymbol{k}_\nu = \left[k_{\nu_1}, \cdots, k_{\nu_P}\right]^{\mathrm{T}} \in \mathbb{R}^{P\times 1}$ and $\boldsymbol{h} = \left[h_1, \cdots, h_P\right]^{\mathrm{T}} \in \mathbb{C}^{P\times 1}$ contain the normalized delay, normalized Doppler and channel gain, respectively. $\boldsymbol{A}\left(\boldsymbol{l}_\tau, \boldsymbol{k}_\nu\right) \in \mathbb{C}^{N\times P}$ can be expressed as

$$\boldsymbol{A}\left(\boldsymbol{l}_\tau, \boldsymbol{k}_\nu\right) = \left[\boldsymbol{a}\left(l_{\tau_1}, k_{\nu_1}\right), \cdots, \boldsymbol{a}\left(l_{\tau_P}, k_{\nu_P}\right)\right], \tag{36}$$

where $\boldsymbol{a}\left(l_{\tau_i}, k_{\nu_i}\right) \in \mathbb{C}^{N\times 1}$, the m-th entry of $\boldsymbol{a}\left(l_{\tau_i}, k_{\nu_i}\right)$ is

$$\left\{\boldsymbol{a}\left(l_{\tau_i}, k_{\nu_i}\right)\right\}_m = \sum_{n=0}^{N-1} x\left(n\right)\mathcal{G}\left(m, n, k_{\nu_i}, l_{\tau_i}\right), \tag{37}$$

where $m \in \{0, \cdots, N-1\}$. It can be seen that $\boldsymbol{A}\left(\boldsymbol{l}_\tau, \boldsymbol{k}_\nu\right)$ contains data, and channel information including k_{ν_i}, l_{τ_i},P, which need to be estimated.

1) Pilot Pattern: Pilots may be inserted into the DAFT domain for efficient CE. Due to the sparsity and compactness of the channel in the DAFT domain, a single pilot can be considered. The arrangement of pilot and data is shown in Fig. 3, which can be expressed as

$$x\left[n\right] = \begin{cases} x_p, & n = n_p \\ 0, & n_p - Q \leqslant n \leqslant n_p + Q, n \neq n_p \\ x_{\mathrm{data}}, & \text{otherwise} \end{cases}, \tag{38}$$

where x_p and x_{data} are single pilot and data, respectively, n_p is the pilot index in the DAFT domain grid, $Q \triangleq \left(l_{\max}+1\right)\left(2\left(k_{\max}+\xi\right)+1\right)-1$ due to the structure of $\mathcal{G}\left(m, n, k_{\nu_i}, l_{\tau_i}\right)$ and the analysis in Section III. The DAFT domain grid within the range $n_p - Q \leqslant n \leqslant n_p + Q, n \neq n_p$ remains null as a guard interval to reduce the mutual interference between data and pilot. Since $\bar{l}_{\tau_i}$ in the equivalent shift $\chi_i = -2Nc_1\bar{l}_{\tau_i} + \bar{k}_{\nu_i}$ is non-negative, the guard intervals on the two sides of the pilot have different lengths. Thus, the right and left guard intervals

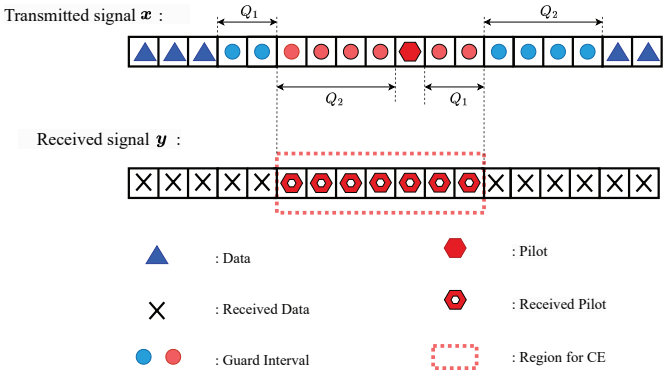

Fig. 3: Single pilot pattern for AFDM systems.

are of lengths $Q_1 = k_{\max} + \xi$ and $Q_2 = Q - Q_1$, respectively. In addition, the two colored guard intervals in Fig. 3 come from pilot and data, respectively.

2) CE Model: Since the main pilot response in $\boldsymbol{y}$ is distributed in the region for CE, truncating the $\boldsymbol{y}$ is intended to reduce complexity. In particular, we employ the received signals $y\left[m\right]$ in the range of $n_p - Q_2 \leqslant m \leqslant n_p + Q_1$ to estimate the channel. Therefore, $y\left[m\right]$ in (13) is simplified to

$$y\left[m\right] = \sum_{i=1}^{P} h_i \mathcal{G}\left(m, n_p, k_{\nu_i}, l_{\tau_i}\right) x_p + z\left[n\right], \tag{39}$$

where $z\left[n\right]$ is the new noise. The matrix form corresponding to (39) is

$$\boldsymbol{y}_{\mathrm{T}} = x_p \boldsymbol{A}_{\mathrm{T}}\left(\boldsymbol{l}_\tau, \boldsymbol{k}_\nu\right)\boldsymbol{h} + \boldsymbol{z}_{\mathrm{T}}, \tag{40}$$

where the subscript T indicates truncation, i.e., $n_p - Q_2 \leqslant m \leqslant n_p + Q_1$. In the truncated $\boldsymbol{A}_{\mathrm{T}}\left(\boldsymbol{l}_\tau, \boldsymbol{k}_\nu\right) \in \mathbb{C}^{(Q+1)\times P}$, $\boldsymbol{a}_{\mathrm{T}}\left(l_{\tau_i}, k_{\nu_i}\right) \in \mathbb{C}^{(Q+1)\times 1}$ is given by

$$\left\{\boldsymbol{a}_{\mathrm{T}}\left(l_{\tau_i}, k_{\nu_i}\right)\right\}_m = \mathcal{G}\left(m, n_p, k_{\nu_i}, l_{\tau_i}\right). \tag{41}$$

3) Decoupling Multipath Estimation: Based on (40), the joint maximum likelihood estimation (JMLE) of $\left(\boldsymbol{l}_\tau, \boldsymbol{k}_\nu, \boldsymbol{h}\right)$ can be expressed as

$$\left(\hat{\boldsymbol{l}}_\tau, \hat{\boldsymbol{k}}_\nu, \hat{\boldsymbol{h}}\right) = \arg\min_{\left(\boldsymbol{l}_\tau, \boldsymbol{k}_\nu, \boldsymbol{h}\right)} \left\|\boldsymbol{y}_{\mathrm{T}} - x_p \boldsymbol{A}_{\mathrm{T}}\left(\boldsymbol{l}_\tau, \boldsymbol{k}_\nu\right)\boldsymbol{h}\right\|^2. \tag{42}$$

According to [45], $\left(\hat{\boldsymbol{l}}_\tau, \hat{\boldsymbol{k}}_\nu\right)$ can be expressed as (43), as shown at the bottom of next page, $\hat{\boldsymbol{h}}$ is given by

$$\hat{\boldsymbol{h}} = \frac{1}{x_p}\left(\boldsymbol{A}_{\mathrm{T}}^{\mathrm{H}}\left(\hat{\boldsymbol{l}}_\tau, \hat{\boldsymbol{k}}_\nu\right)\boldsymbol{A}_{\mathrm{T}}\left(\hat{\boldsymbol{l}}_\tau, \hat{\boldsymbol{k}}_\nu\right)\right)^{-1}\boldsymbol{A}_{\mathrm{T}}^{\mathrm{H}}\left(\hat{\boldsymbol{l}}_\tau, \hat{\boldsymbol{k}}_\nu\right)\boldsymbol{y}_{\mathrm{T}}. \tag{44}$$

Theorem 2. For any $i \neq j$, $\left\|\boldsymbol{a}_{\mathrm{T}}\left(l_{\tau_i}, k_{\nu_i}\right)\right\|^2 = 1$, $\left|\boldsymbol{a}_{\mathrm{T}}^{\mathrm{H}}\left(l_{\tau_i}, k_{\nu_i}\right)\boldsymbol{a}_{\mathrm{T}}\left(l_{\tau_j}, k_{\nu_j}\right)\right| \ll 1$.

Remark 1. According to Theorem 2, $\boldsymbol{A}_{\mathrm{T}}^{\mathrm{H}}\left(\boldsymbol{l}_\tau, \boldsymbol{k}_\nu\right)\boldsymbol{A}_{\mathrm{T}}\left(\boldsymbol{l}_\tau, \boldsymbol{k}_\nu\right)$ is approximately the identity matrix $\boldsymbol{I}_P$.

Proof: The proof is given in Appendix B. ■

Thus, (43) and (44) can be well approximated as

$$\left(\hat{\boldsymbol{l}}_\tau, \hat{\boldsymbol{k}}_\tau\right) \approx \arg\max_{\left(\boldsymbol{l}_\tau, \boldsymbol{k}_\nu\right)} \sum_{i=1}^{P} \left|\boldsymbol{a}_{\mathrm{T}}^{\mathrm{H}}\left(l_{\tau_i}, k_{\nu_i}\right)\boldsymbol{y}_{\mathrm{T}}\right|^2, \tag{45}$$

$$\hat{\boldsymbol{h}} \approx \frac{\boldsymbol{A}_{\mathrm{T}}^{\mathrm{H}}\left(\hat{\boldsymbol{l}}_{\tau}, \hat{\boldsymbol{k}}_{\nu}\right) \boldsymbol{y}_{T}}{x_{p}}. \tag{46}$$

Since $\boldsymbol{a}_{\mathrm{T}}\left(l_{\tau_i}, k_{\nu_i}\right)$ and $\boldsymbol{a}_{\mathrm{T}}\left(l_{\tau_j}, k_{\nu_j}\right)$ are approximately orthogonal, they exhibit path separability, where $i \neq j$. The separability of the two paths improves as N increases. In addition, $\boldsymbol{y}_{\mathrm{T}} = \sum_{i=1}^{P} x_p h_i \boldsymbol{a}_{\mathrm{T}}\left(l_{\tau_i}, k_{\nu_i}\right)$. Therefore, $\left(h_i, l_{\tau_i}, k_{\nu_i}\right)$ of each path can be estimated separately.

Therefore, based on the separability of the channel in the DAFT domain, the joint estimation of parameters for all paths can be decoupled. The estimation result for the i-th path is

$$\left(\hat{l}_{\tau_i}, \hat{k}_{\nu_i}\right) \approx \arg \max_{\left(l_{\tau}, k_{\nu}\right)} \left|\boldsymbol{a}_{\mathrm{T}}^{\mathrm{H}}\left(l_{\tau}, k_{\nu}\right) \boldsymbol{y}_{T}\right|^{2}, \tag{47}$$

$$\hat{h}_i \approx \frac{1}{x_p} \boldsymbol{a}_{\mathrm{T}}^{\mathrm{H}}\left(\hat{l}_{\tau_i}, \hat{k}_{\nu_i}\right) \boldsymbol{y}_{T}. \tag{48}$$

B. MF CE for FDFD channels

For (47), $\left(\hat{l}_{\tau_i}, \hat{k}_{\nu_i}\right)$ can be obtained by searching for consecutive $\left(l_{\tau_i}, k_{\nu_i}\right)$. Specifically, since $\boldsymbol{a}_{\mathrm{T}}\left(l_{\tau_i}, k_{\nu_i}\right)$ in $\boldsymbol{y}_{\mathrm{T}}$ and $\boldsymbol{a}_{\mathrm{T}}\left(l_{\tau}, k_{\nu}\right)$ have the same structure, it can be anticipated that $\left|\boldsymbol{a}_{\mathrm{T}}^{\mathrm{H}}\left(l_{\tau}, k_{\nu}\right) \boldsymbol{y}_{T}\right|$ achieves its maximum value at $\left(l_{\tau}, k_{\nu}\right) = \left(l_{\tau_i}, k_{\nu_i}\right)$. However, the complexity of searching for $\left(\hat{l}_{\tau_i}, \hat{k}_{\nu_i}\right)$ in space $\{[0, l_{\max}] \times [-k_{\max}, k_{\max}]\}$ is still high. A simple and effective method is to estimate $\left(\bar{l}_{\tau_i}, \bar{k}_{\nu_i}\right)$ of the path based on the maximum peaks in the received signal $\boldsymbol{y}_{\mathrm{T}}$, i.e.,

$$\hat{\bar{l}}_{\tau_i} = \lfloor \frac{\hat{\chi}_i}{-2Nc_1} \rceil, \hat{\bar{k}}_{\nu_i} = \hat{\chi}_i + 2Nc_1 \hat{\bar{l}}_{\tau_i}, \tag{49}$$

where $\hat{\chi}_i = m_{\max} - n_p$, $m_{\max} = \underset{m}{\operatorname{argmax}} |y[m]|$.

The fractional $\left(\hat{\iota}_{\tau_i}, \hat{\kappa}_{\nu_i}\right)$ can be obtained by a global search within a small continuous region $\{[-0.5, 0.5] \times [-0.5, 0.5]\}$. Therefore, $\left(\hat{\iota}_{\tau_i}, \hat{\kappa}_{\nu_i}\right)$ can be expressed as

$$\left(\hat{\iota}_{\tau_i}, \hat{\kappa}_{\nu_i}\right) = \arg \max_{\left(\iota_{\tau}, \kappa_{\nu}\right) \in \boldsymbol{\Omega}} \left|\boldsymbol{a}_{\mathrm{T}}^{\mathrm{H}}\left(\hat{\bar{l}}_{\tau_i} + \iota_{\tau}, \hat{\bar{k}}_{\nu_i} + \kappa_{\nu}\right) \boldsymbol{y}_{T}\right|^{2}, \tag{50}$$

where $\boldsymbol{\Omega} = \{\boldsymbol{\Gamma} \times \boldsymbol{\Gamma}\} \in \mathbb{R}^{(\rho+1)\times(\rho+1)}$, $\Gamma_{\tilde{n}} = -0.5 + \frac{1}{\rho}\tilde{n}, \tilde{n} \in [0, \rho]$, ρ is the size of the search step.

To further reduce the complexity, a decoupled DD estimation can be considered, i.e.,

$$\hat{\iota}_{\tau_i} = \arg \max_{\iota_{\tau} \in \boldsymbol{\Gamma}} \left|\boldsymbol{a}_{\mathrm{T}}^{\mathrm{H}}\left(\hat{\bar{l}}_{\tau_i} + \iota_{\tau}, \hat{\bar{k}}_{\nu_i}\right) \boldsymbol{y}_{T}\right|^{2}, \tag{51}$$

$$\hat{\kappa}_{\nu_i} = \arg \max_{\kappa_{\nu} \in \boldsymbol{\Gamma}} \left|\boldsymbol{a}_{\mathrm{T}}^{\mathrm{H}}\left(\hat{\bar{l}}_{\tau_i} + \hat{\iota}_{\tau_i}, \hat{\bar{k}}_{\nu_i} + \kappa_{\nu}\right) \boldsymbol{y}_{T}\right|^{2}. \tag{52}$$

Compared with the joint DD estimation in (50), which requires $(\rho+1)^2$ searches, the decoupled DD estimation in (51)–(52) involves only $2(\rho+1)$ searches. To distinguish between the joint DD estimation and the decoupled DD estimation, they are referred to as MF-JE and MF-DE, respectively.

Noted that $\left(\hat{h}_i, \hat{l}_{\tau_i}, \hat{k}_{\nu_i}\right)$ in (48)-(52) represent the estimation results for single path. For multiple paths, an iterative estimation scheme is required. Specifically, the signal corresponding to $\left(\hat{l}_{\tau}^{(t)}, \hat{k}_{\nu}^{(t)}, \hat{h}^{(t)}\right)$ in the (t)-th iteration is

$$\boldsymbol{y}_{\mathrm{T}}^{(t),t} = x_p \hat{h}^{(t)} \boldsymbol{a}_{\mathrm{T}}\left(\hat{l}_{\tau}^{(t)}, \hat{k}_{\nu}^{(t)}\right) \in \mathbb{C}^{(Q+1)\times 1}. \tag{53}$$

Before estimating the next path, $\boldsymbol{y}_{\mathrm{T}}^{(t),t}$ is subtracted from the received signal $\boldsymbol{y}_{\mathrm{T}}^{(t)}$, i.e.,

$$\boldsymbol{y}_{\mathrm{T}}^{(t+1)} = \boldsymbol{y}_{\mathrm{T}}^{(t)} - \boldsymbol{y}_{\mathrm{T}}^{(t),t}. \tag{54}$$

The iteration terminates if the maximum number T_{iter} is reached or $\left|\left\|\boldsymbol{y}_{\mathrm{T}}^{(t+1)}\right\| - \left\|\boldsymbol{y}_{\mathrm{T}}^{(t)}\right\|\right| / \left\|\boldsymbol{y}_{\mathrm{T}}^{(t)}\right\| \leqslant \sigma$, where the preset threshold $\sigma > 0$. The MF with joint DD estimation (MF-JE) CE scheme is summarized in **Algorithm** 1.

Algorithm 1 Proposed MF-JE and MF-DE CE scheme for FDFD channels

Input: Received signal $\boldsymbol{y}_{\mathrm{T}}$.

Initialization: $\boldsymbol{y}_{\mathrm{T}}^{(t)} = \boldsymbol{y}_{\mathrm{T}}$, the maximum number of iterations T_{iter}, threshold σ, $l_{\max}$, $k_{\max}$, $\hat{\boldsymbol{l}}_{\tau} = [], \hat{\boldsymbol{k}}_{\nu} = [], \hat{\boldsymbol{h}} = [], t = 1$.

1: **repeat**
2: According to (49), $\left(\bar{l}_{\tau}^{(t)}, \bar{k}_{\nu}^{(t)}\right)$ is obtained.
3: $\left(\hat{\iota}_{\tau}^{(t)}, \hat{\kappa}_{\nu}^{(t)}\right)$ is estimated via (50) in MF-JE and via (51)–(52) in MF-DE.
4: $\hat{h}^{(t)}$ can be obtained by (48).
5: $\hat{\boldsymbol{l}}_{\tau} = \left[\hat{\boldsymbol{l}}_{\tau}, \hat{l}_{\tau}^{(t)}\right], \hat{\boldsymbol{k}}_{\nu} = \left[\hat{\boldsymbol{k}}_{\nu}, \hat{k}_{\nu}^{(t)}\right], \hat{\boldsymbol{h}} = \left[\hat{\boldsymbol{h}}, \hat{h}^{(t)}\right]$.
6: The $\boldsymbol{y}_{\mathrm{T}}^{(t+1)}$ is obtained by (54).
7: $t = t + 1$.
8: until $t = T_{\mathrm{iter}}$ or $\left|\frac{\left\|\boldsymbol{y}_{\mathrm{T}}^{(t+1)}\right\| - \left\|\boldsymbol{y}_{\mathrm{T}}^{(t)}\right\|}{\left\|\boldsymbol{y}_{\mathrm{T}}^{(t)}\right\|}\right| \leqslant \sigma$.

Output: $\left(\hat{\boldsymbol{l}}_{\tau}, \hat{\boldsymbol{k}}_{\nu}, \hat{\boldsymbol{h}}\right)$.

C. MF-GFS-DE CE for FDFD channels

In Subsection IV-B, an MF CE scheme is proposed. However, the trade-off between the complexity and estimation performance of the MF CE scheme still depends on the ρ. Performing a global search over an interval is inefficient, and the estimation accuracy is limited by the search step size ρ. The larger the ρ, the finer the grid $\boldsymbol{\Gamma}$, enabling more accurate estimation of fractional part at the cost of higher complexity. To address this issue, we introduce a MF-GFS CE scheme based on the GFS algorithm in this subsection. The GFS algorithm unevenly divides the search interval into two parts through the ratio of two consecutive generalized Fibonacci numbers (GFNs) to achieve an efficient search. The i-th GFN is denoted by $S_i(a, b, p, q)$, where $S_0 = a$, $S_1 = b$, $S_{i+2} = pS_{i+1} + qS_i$, i is a non-negative integer, a and b be two non-negative integers such that $a + b > 0$, p and q be two positive integers.

$$\left(\hat{\boldsymbol{l}}_{\tau}, \hat{\boldsymbol{k}}_{\nu}\right) = \arg \max_{\left(\boldsymbol{l}_{\tau}, \boldsymbol{k}_{\nu}\right)} \boldsymbol{y}_{\mathrm{T}}^{\mathrm{H}} \boldsymbol{A}_{\mathrm{T}}\left(\boldsymbol{l}_{\tau}, \boldsymbol{k}_{\nu}\right) \left(\boldsymbol{A}_{\mathrm{T}}^{\mathrm{H}}\left(\boldsymbol{l}_{\tau}, \boldsymbol{k}_{\nu}\right) \boldsymbol{A}_{\mathrm{T}}\left(\boldsymbol{l}_{\tau}, \boldsymbol{k}_{\nu}\right)\right)^{-1} \boldsymbol{A}_{\mathrm{T}}^{\mathrm{H}}\left(\boldsymbol{l}_{\tau}, \boldsymbol{k}_{\nu}\right) \boldsymbol{y}_{\mathrm{T}}. \tag{43}$$

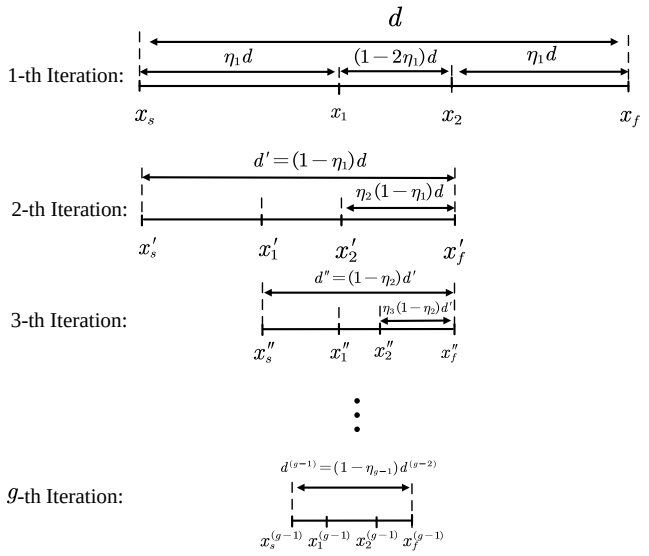

Fig. 4: The diagram of the GFS algorithm.

Note that an important pre-condition for using the GFS algorithm is that the objective function should be a bounded unimodal function. Since fractional delays may cause local peaks, the objective functions in both (50) and (51) are generally not unimodal.

Theorem 3. In (52), $\left|\boldsymbol{a}_{\mathrm{T}}^{\mathrm{H}}\left(\hat{\bar{l}}_{\tau_i}+\hat{\iota}_{\tau_i},\hat{\bar{k}}_{\nu_i}+\kappa_\nu\right)\boldsymbol{y}_T\right|^2$ is a bounded unimodal function.

Proof: The proof is given in Appendix C. ■

After dividing the search interval by two consecutive GFNs, the interval of uncertainty (IU) containing the optimal value κ_{ν_i} needs to be determined. For convenience, assume that the search interval is $[x_s, x_f]$, and $x_s < x_1 < x_2 < x_f$. The new IU $\left[x_s', x_f'\right]$ can be expressed as

$$\left[x_s', x_f'\right] = \begin{cases} [x_s, x_2], & f(x_1) < f(x_2) \\ [x_1, x_f], & f(x_1) > f(x_2) \end{cases}. \tag{55}$$

The process of the GFS for estimating $\hat{\kappa}_{\nu_i}$ is shown in Fig. 4. Note that it is necessary to set a maximum GFN S_{N_G}, $N_G = T_G + 2$, which determines the maximum number of iterations, T_G, for the GFS. For the g-th iteration, the IU is divided based on the ratio of two successive higher GFNs, i.e.,

$$\eta_g = \frac{qS_{N_G-(g+1)}(a,b,p,q)}{S_{N_G-(g-1)}(a,b,p,q)}, \tag{56}$$

where $g \in [1, T_G]$. η_g can determine the positions of $x_1^{(g-1)}$ and $x_2^{(g-1)}$. In general, for the g-th iteration, the size of IU is

$$d^{(g-1)} = (1-\eta_{g-1})\, d^{(g-2)}. \tag{57}$$

Then, the new IU can be obtained by (55). The iteration will terminate if the maximum number T_G is reached or

$$d^{(g-1)} = \left|x_f^{(g-1)} - x_s^{(g-1)}\right| < \varepsilon, \tag{58}$$

where ε is the pre-set threshold. At this moment, if there is no additional prior, fractional part can be estimated as

$$\hat{\kappa}_{\nu_i} = \frac{x_s^{(g-1)} + x_f^{(g-1)}}{2}. \tag{59}$$

The proposed GFS algorithm for estimating $\hat{\kappa}_{\nu_i}$ is summarized in **Algorithm** 2. Except for $\hat{\kappa}_{\nu_i}$, the MF-GFS scheme follows the same procedure as the MF scheme. For the MF-GFS scheme, $\hat{\kappa}_{\nu_i}$ is obtained via the **Algorithm** 2 rather than (52).

Note that the size of IU in the global search method is $\frac{1}{\rho+1}$, which is generally on the magnitude of 10^{-1} or 10^{-2}. However, the size of IU in the GFS is several orders of magnitude smaller. Therefore, the proposed MF-GFS scheme is generally more effective than the MF scheme.

Algorithm 2 The proposed GFS Algorithm

Input: Received signal $\boldsymbol{y}_{\mathrm{T}}$, the objective function $f(\kappa_\nu) = \left|\boldsymbol{a}_{\mathrm{T}}^{\mathrm{H}}\left(\hat{\bar{l}}_{\tau_i}+\hat{\iota}_{\tau_i},\hat{\bar{k}}_{\nu_i}+\kappa_\nu\right)\boldsymbol{y}_T\right|^2$.

Initialization: $g=1$, T_G, IU $\left[x_s^{(0)}, x_f^{(0)}\right] = [-0.5, 0.5]$.

1: **repeat**
2: From (57) and (56), $x_1^{(g-1)}$ and $x_2^{(g-1)}$ are obtained.
3: According to (55), the new IU $\left[x_s^{(g)}, x_f^{(g)}\right]$ is obtained.
4: $g = g+1$.
5: **until** $g = T_G$ or $d^{(g-1)} = \left|x_f^{(g-1)} - x_s^{(g-1)}\right| < \varepsilon$.
6: Calculate $\hat{\kappa}_{\nu_i}$ according to (59).

Output: $\hat{\kappa}_{\nu_i}$.

Algorithm 3 The proposed MF and MF-GFS CE scheme for IDFD channels

Input: Received signal $\boldsymbol{y}_{\mathrm{T}}$, the objective function $\left|\boldsymbol{a}_{\mathrm{T}}^{\mathrm{H}}\left(\hat{\bar{l}}_{\tau_i}+\hat{\iota}_{\tau_i},\hat{\bar{k}}_{\nu_i}+\kappa_\nu\right)\boldsymbol{y}_T\right|^2$.

Initialization: $\boldsymbol{y}_{\mathrm{T}}^{(t)} = \boldsymbol{y}_{\mathrm{T}}$, the maximum number of iterations T_{iter} and T_G, threshold σ and ϵ, $l_{\max}$, $k_{\max}$, $\hat{\boldsymbol{l}}_\tau = [], \hat{\boldsymbol{k}}_\nu = [], \hat{\boldsymbol{h}} = []$, $t=1$.

1: **repeat**
2: According to (49), $\left(\hat{\bar{l}}_\tau^{(t)}, \hat{\bar{k}}_\nu^{(t)}\right)$ for a path is obtained.
3: $\hat{\kappa}_\nu^{(t)}$ is estimated via (60) in MF and via **Algorithm** 2 in MF-GFS.
4: $\hat{h}^{(t)}$ can be obtained by (48).
5: $\hat{\boldsymbol{l}}_\tau = \left[\hat{\boldsymbol{l}}_\tau, \hat{l}_\tau^{(t)}\right]$, $\hat{\boldsymbol{k}}_\nu = \left[\hat{\boldsymbol{k}}_\nu, \hat{k}_\nu^{(t)}\right]$, $\hat{\boldsymbol{h}} = \left[\hat{\boldsymbol{h}}, \hat{h}^{(t)}\right]$.
6: $\boldsymbol{y}_{\mathrm{T}}^{(t+1)}$ is obtained by (54).
7: $t = t+1$.
8: until $t = T_{\mathrm{iter}}$ or $\left|\frac{\left\|\boldsymbol{y}_{\mathrm{T}}^{(t+1)}\right\| - \left\|\boldsymbol{y}_{\mathrm{T}}^{(t)}\right\|}{\left\|\boldsymbol{y}_{\mathrm{T}}^{(t)}\right\|}\right| \leqslant \sigma$.

Output: $\left(\hat{\boldsymbol{l}}_\tau, \hat{\boldsymbol{k}}_\nu, \hat{\boldsymbol{h}}\right)$.

D. MF and MF-GFS CE schemes for IDFD channels

In typical wide-band systems such as satellite or millimeter-wave communications, B is sufficiently large to approximate τ_i to the nearest sampling point [6]. Therefore, MF and MF-GFS schemes are proposed for IDFD channels.

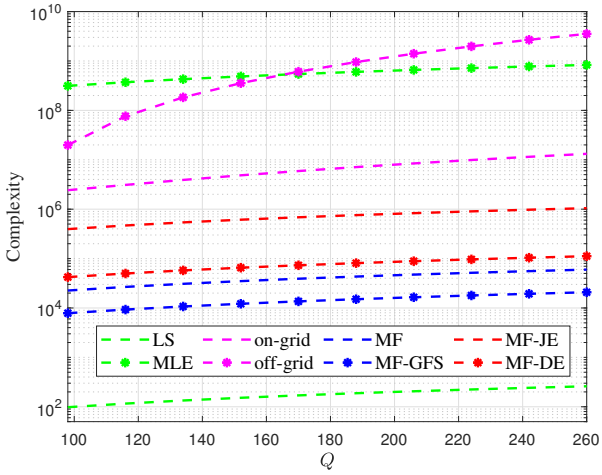

Fig. 5: Complexity comparison of different CE schemes.

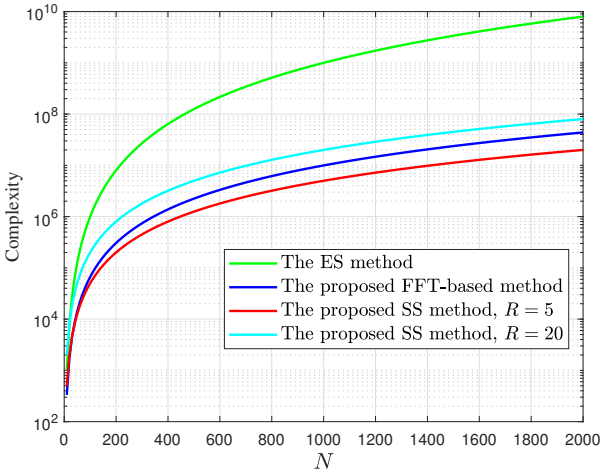

Fig. 6: Complexity of constructing $\boldsymbol{H}_{\text{eff}}$ via different methods.

The observation model in (40) is still considered. The estimation of $\left(h_i, l_{\tau_i} = \bar{l}_{\tau_i}, k_{\nu_i} = \bar{k}_{\nu_i} + \kappa_{\nu_i}\right)$ for the i-th path can also be expressed as (47) and (48).

To reduce complexity, the integer $\left(\bar{l}_{\tau_i}, \bar{k}_{\nu_i}\right)$ is initially also estimated using (49). $\hat{\kappa}_{\nu_i}$ can be expressed as

$$\hat{\kappa}_{\nu_i} = \arg\max_{\kappa_\nu \in \boldsymbol{\Gamma}} \left| \boldsymbol{a}_{\mathrm{T}}^{\mathrm{H}} \left(\hat{\bar{l}}_{\tau_i}, \hat{\bar{k}}_{\nu_i} + \kappa_\nu \right) \boldsymbol{y}_T \right|^2. \tag{60}$$

The MF scheme is to directly search the grid $\boldsymbol{\Gamma}$ to get $\hat{\kappa}_{\nu_i}$. In addition, $\left| \boldsymbol{a}_{\mathrm{T}}^{\mathrm{H}} \left(\hat{\bar{l}}_{\tau_i}, \hat{\bar{k}}_{\nu_i} + \kappa_\nu \right) \boldsymbol{y}_T \right|^2$ is a bounded unimodal function, achieving its extreme value at $\kappa_\nu = \kappa_{\nu_i}$. This proof is similar to Appendix C. Therefore, to reduce complexity and improve performance, **Algorithm** 2 is used to estimate $\hat{\kappa}_{\nu_i}$. Note that the same iterative method is also considered for parameter estimation of multiple paths, which estimates one path in one iteration. The proposed MF and MF-GFS CE schemes for IDFD channels are summarized in **Algorithm** 3.

E. Complexity Analysis

In this subsection, we analyze complexity of the proposed MF and MF-GFS CE schemes. For the MF CE in the IDFD channels, The complexity of (49) is $\mathcal{O}(Q)$. In addition, based on (60), estimating $\hat{\kappa}_{\nu_i}$ requires $\mathcal{O}(Q\rho)$. Calculating (48) costs $\mathcal{O}(Q)$. To calculate $\boldsymbol{y}_{\mathrm{T}}^{(t+1)}$ in (54), $\mathcal{O}(Q)$ are required. Therefore, the complexity in each iteration is $\mathcal{O}(Q\rho + 3Q)$. For the proposed MF-GFS CE scheme in the IDFD channel, estimating $\hat{\kappa}_{\nu_i}$ through **Algorithm** 2 costs $\mathcal{O}(T_G Q)$. Therefore, the complexity in each iteration is $\mathcal{O}(T_G Q + 3Q)$. The remaining analysis is similar to the MF scheme. The complexity is summarized in Table I, where L is the number of columns in the measurement matrix for the CS schemes. Fig. 5 is the complexity comparison, where $l_{\max} = 8$, $k_{\max} \in [2, 10]$. one can see the low-complexity nature of the proposed schemes.

V. Simulation Results

In this section, the CE performances of the proposed MF and MF-GFS methods are evaluated. Unless otherwise stated, the simulation parameters are shown in Table II. τ_i and ν_i are randomly and uniformly generated within $[0, \tau_{\max}]$ and $[-\nu_{\max}, \nu_{\max}]$, respectively. The system signal-to-noise ratio (SNR) is defined as $\frac{E\{|x[n]|^2\}}{\sigma^2}$. For the pilot x_p, $10\log_{10}\frac{|x_p|^2}{E\{|x[n]|^2\}} = 30$ dB is satisfied. For the proposed algorithms, set $T_{\text{iter}} = 15$, $\sigma = 10^{-3}$, $\rho = 20$. For comparison, we consider the traditional LS scheme [37], the MLE scheme [16], the on-grid scheme [38], [39] with OMP algorithm, and the off-grid scheme [40]. For CE schemes based on CS algorithm, the grid resolution is 0.5. We reconstruct $\hat{\boldsymbol{H}}_{\text{eff}}$ using the estimated parameters, and define NMSE as $\text{NMSE} = \| \boldsymbol{H}_{\text{eff}} - \hat{\boldsymbol{H}}_{\text{eff}} \|^2 / \| \boldsymbol{H}_{\text{eff}} \|^2$.

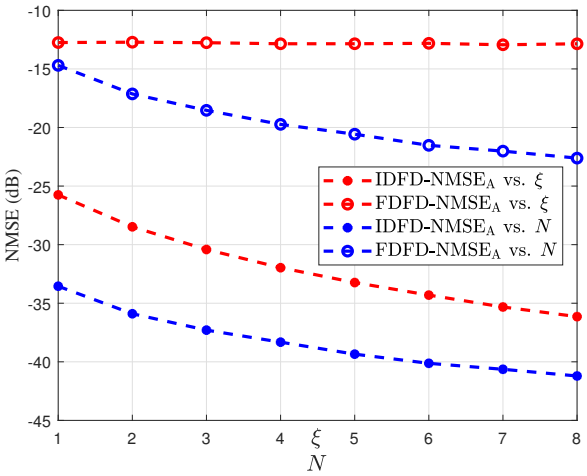

Fig. 7: Orthogonality of $\boldsymbol{A}_{\mathrm{T}}(\boldsymbol{l}_\tau, \boldsymbol{k}_\nu)$ vs. ξ and N.

Fig. 6 shows a comparison of the complexity of constructing $\boldsymbol{H}_{\text{eff}}$ using different methods. For large N, the proposed FFT-based and SS methods reduce complexity by at least two orders of magnitude. The SS method is preferable for small R, while the FFT-based method is better for large R.

The approximate orthogonality of $\boldsymbol{A}_{\mathrm{T}}(\boldsymbol{l}_\tau, \boldsymbol{k}_\nu)$ for different values of ξ and N is shown in Fig. 7. For "NMSE$_{\text{A}}$ vs. ξ", we consider $N = 256$, $\xi \in [1, 8]$. For "NMSE$_{\text{A}}$ vs.

TABLE I: COMPARISON OF COMPLEXITY

Method	Complexity
LS scheme [37]	$\mathcal{O}(Q)$
MLE scheme [16]	$\mathcal{O}(\rho^P Q)$
on-grid scheme [38], [39]	$\mathcal{O}(T_{\text{iter}}^3 + T_{\text{iter}} LQ + T_{\text{iter}}^2 Q)$
off-grid scheme [40]	$\mathcal{O}(T_{\text{iter}} L^2 Q)$
The proposed MF scheme for IDFD channels	$\mathcal{O}(T_{\text{iter}}(\rho Q + 3Q))$
The proposed MF-GFS scheme for IDFD channels	$\mathcal{O}(T_{\text{iter}}(T_G Q + 3Q))$
The proposed MF-JE and MF-DE scheme for FDFD channels	$\mathcal{O}(T_{\text{iter}}(\rho^2 Q + 3Q))$, $\mathcal{O}(T_{\text{iter}}(2\rho Q + 3Q))$
The proposed MF-GFS-DE scheme for FDFD channels	$\mathcal{O}(T_{\text{iter}}(\rho + T_G) Q + 3Q)$

TABLE II: SIMULATION PARAMETERS

Parameter	Value
The number of chirp-carriers	$N = 256$
Carrier frequency	4 GHz
The channel coefficient	$h_i \sim \mathcal{CN}(0, \frac{1}{P})$
Maximum delay	$\tau_{\max} = 1.56 \times 10^{-5}$s
Maximum relative velocity	540 km/h
Maximum Doppler shift	2×10^3 Hz
Subcarrier spacing	$\Delta f = 1$ kHz
Number of channel paths	$P = 5$
Data modulation	4-QAM
ξ, ξ'	4, 5

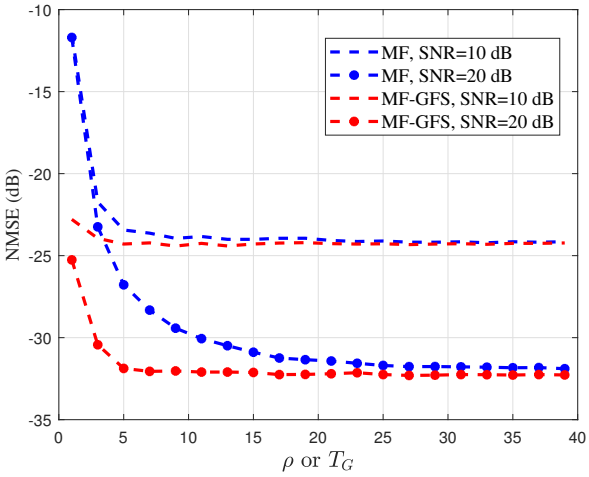

Fig. 8: Effects of ρ on MF CE and T_G on MF-GFS CE.

N", we have $\xi = 4$, $N \in 200 \times [1, 8]$. To make this orthogonality more obvious, the integer parts of the delays for different paths are set to differ. Note that $\text{NMSE}_{\text{A}} = \| \boldsymbol{I} - \boldsymbol{A}_{\text{T}}^{\text{H}}(\boldsymbol{l}_\tau, \boldsymbol{k}_\nu) \boldsymbol{A}_{\text{T}}(\boldsymbol{l}_\tau, \boldsymbol{k}_\nu) \|^2 / \|\boldsymbol{I}\|^2$. It can be observed that this approximate orthogonality is still good enough even in fractional channels. This orthogonality improves with the increase of ξ or N. However, for FDFD channels, increasing ξ does not improve orthogonality.

Fig. 8 shows the effects of ρ on MF and T_G on MF-GFS CE for IDFD channel. Compared to the MF CE scheme, the MF-GFS CE scheme can achieve better performance with lower complexity. Fig. 9 shows the BER performance of the proposed MF scheme for IDFD channel with different SNR and ρ. The BER is obtained by LMMSE algorithm. As ρ increases, the size of the IU correspondingly decreases, enabling more accurate estimation of the fractional Doppler, which leads to improvements in both NMSE and BER.

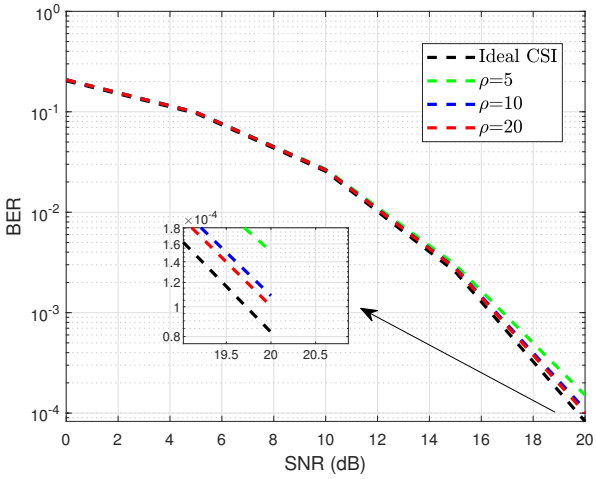

Fig. 9: BER comparison of the proposed MF scheme versus SNR for different ρ values.

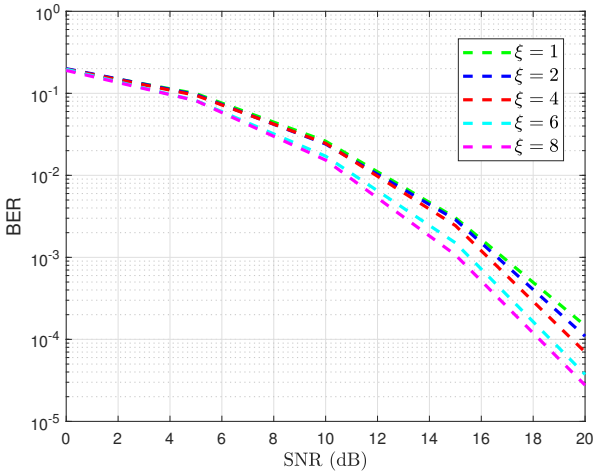

Fig. 10: BER comparison of the proposed MF scheme versus SNR for different ξ values.

The impact of different ξ on the BER of the MF scheme is shown in Fig. 10. It can be observed that the BER improves as ξ increases. In this case, the interference between different paths will decrease, making the estimated parameters more accurate, and hence improving BER performance. In addition, according to Fig. 7, as ξ increases, the orthogonality performance of $\boldsymbol{A}_{\text{T}}(\boldsymbol{l}_\tau, \boldsymbol{k}_\nu)$ is improved, thus leading to further improved CE and BER performances.

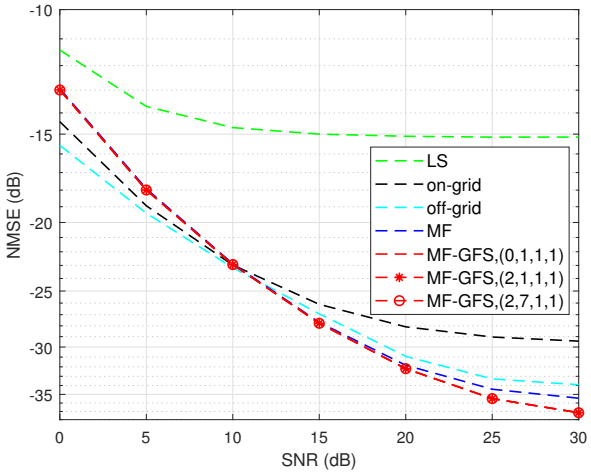

Fig. 11: Comparison of NMSE performance.

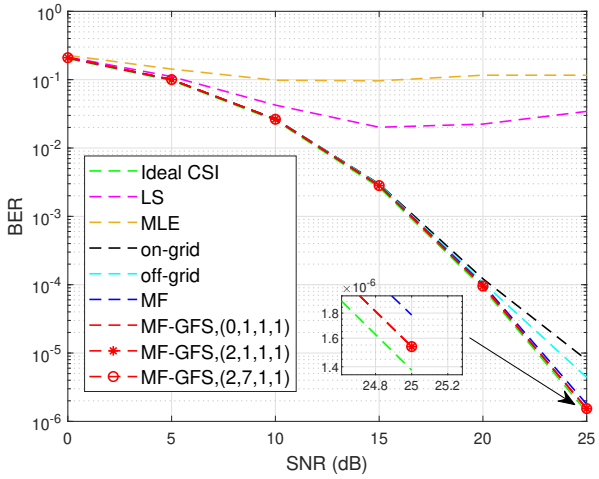

Fig. 12: Comparison of BER performance.

The NMSE and BER performances of different schemes for IDFD channels are compared in Fig. 11 and Fig. 12, respectively. We set $\rho = 15$ and $T_G = 8$. In addition, the performance of the MF-GFS scheme with different GFN, distinguished by (a, b, p, q), is also compared. The performance of the proposed MF scheme and MF-GFS scheme are significantly improved compared to that of other schemes. Since the size of the IU estimated by the MF-GFS scheme is significantly smaller than that of MF, it can be seen that the performance of the proposed MF-GFS scheme outperforms that of the MF scheme at high SNR. In addition, since the ratio of two consecutive GFNs is generally close to the golden ratio, different GFNs yield similar IU divisions, thereby resulting in a negligible impact on the performance of the MF-GFS scheme.

Fig. 13 is a comparison of BER performance for FDFD channels. As analyzed in subsection III-B-3), local peaks induced by ι_{τ_i} exacerbate ICCI and inter-path interference, leading to deteriorated CE and BER performances. However, the proposed MF CE scheme outperforms existing schemes.

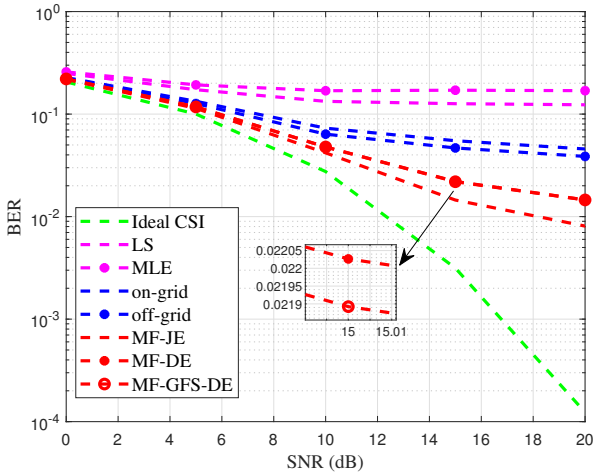

Fig. 13: Comparison of BER performance for FDFD channels.

VI. Conclusions

This paper has studied an MF-based CE scheme for AFDM systems, by upholding the key idea of sequentially estimating the parameters of each path. After analyzing the channel in the DAFT domain, we proposed two low-complexity methods to construct the channel matrix by exploiting the inherent structural properties of the channel matrix, reducing complexity by at least two orders of magnitude. We have proposed the MF-JE CE scheme, which decouples multipath estimation by exploiting path orthogonality and separability. Furthermore, to further reduce redundant computation in estimating fractional parameters, the MF-GFS-DE CE scheme was developed. This scheme incorporated the GFS algorithm and decoupled joint DD estimation at the cost of a slight performance loss. Both schemes are extended to the typical broadband systems. The simulation results showed that the proposed schemes offer more significant advantages over existing CE schemes in terms of improved communication performances and lower complexities.

Appendix A
Proof of Theorem 1

To analyze the impact of each path, a more detailed I/O relationship is required. Considering the noise-free version of (11), its corresponding discrete-time signal expression is

$$r[\bar{n}] = \frac{1}{\sqrt{N}} \sum_{i=0}^{P-1} h_i \sum_{n=0}^{N-1} x[n] e^{\frac{j2\pi}{N} k_{\nu_i}(\bar{n}-l_{\tau_i})} \times e^{j2\pi\left(c_2 n^2 + c_1(\bar{n}-l_{\tau_i})^2 + \frac{n}{N}(\bar{n}-l_{\tau_i}) + d_{\bar{n},n}\iota_{\tau_i}\right)}, \tag{61}$$

where $d_{\bar{n},n} = \sum_{q=0}^{2Nc_1} \beta_{\bar{n},n}(q)$, $\beta_{\bar{n},n}(q)$ is given by

$$\beta_{\bar{n},n}(q) = \begin{cases} q, & \lfloor \frac{t_{n,q}}{T_s} \rfloor + 1 \le \bar{n} \le \lfloor \frac{t_{n,q+1}}{T_s} \rfloor \\ 0, & \text{otherwise} \end{cases}. \tag{62}$$

Note that once N and c_1 are fixed, $d_{\bar{n},n}$ is determined and can thus be pre-calculated. Substituting (61) and the DAFT kernel $\phi_m(t)$ into (12), The noise-free version of $y[m]$ can

$$y[m]=\sum_{n=0}^{N-1}x[n]\left[\sum_{i=1}^{P}h_i\underbrace{e^{\frac{-j2\pi}{N}\left(-Nc_1l_{\tau_i}^2+\left(n+k_{\nu_i}\right)l_{\tau_i}+Nc_2\left(m^2-n^2\right)\right)}}_{\alpha\left(m,n,l_{\tau_i},k_{\nu_i}\right)}\underbrace{\frac{1}{N}\sum_{\bar{n}=0}^{N-1}e^{\frac{-j2\pi}{N}\left(m-n+2Nc_1l_{\tau_i}-k_{\nu_i}\right)\bar{n}-Nd_{\bar{n},n}\iota_{\tau_i}}}_{\mathcal{F}\left(m,n,l_{\tau_i},k_{\nu_i}\right)}\right], \tag{63}$$

$$=\sum_{n=0}^{N-1}x[n]\,H_{\text{eff}}[m,n]+w[n]. \tag{64}$$

$$\left|\boldsymbol{a}_i^{\mathrm{H}}\boldsymbol{a}_j\right|=\left|\sum_{m=0}^{N-1}\frac{1}{N}\sum_{n_i=0}^{N-1}e^{\frac{j2\pi}{N}\left((m-n_p+2Nc_1l_{\tau_i}-k_{\nu_i})n_i-Nd_{n_i,n_p}\iota_{\tau_i}\right)}\frac{1}{N}\sum_{n_j=0}^{N-1}e^{\frac{-j2\pi}{N}\left((m-n_p+2Nc_1l_{\tau_j}-k_{\nu_j})n_j-Nd_{n_j,n_p}\iota_{\tau_j}\right)}\right| \tag{65}$$

$$=\frac{1}{N}\left|\sum_{n_i=0}^{N-1}\sum_{n_j=0}^{N-1}e^{\frac{-j2\pi}{N}\left[-n_p(n_j-n_i)+2Nc_1(l_{\tau_j}n_j-l_{\tau_i}n_i)-\left(k_{\nu_j}n_j-k_{\nu_i}n_i\right)-N\left(d_{n_j,n_p}\iota_{\tau_j}-d_{n_i,n_p}\iota_{\tau_i}\right)\right]}\underbrace{\frac{1}{N}\sum_{m=0}^{N-1}e^{\frac{-j2\pi}{N}m(n_j-n_i)}}_{\delta(n_j-n_i)}\right|. \tag{66}$$

be expressed as (63). Finally, the square bracket in (63) is replaced by $H_{\text{eff}}[m,n]$, which completes the proof.

Appendix B
Proof of Theorem 2

For simplicity, we use $\left|\boldsymbol{a}_i^{\mathrm{H}}\boldsymbol{a}_j\right|$ to represent $\left|\boldsymbol{a}_{\mathrm{T}}^{\mathrm{H}}\left(l_{\tau_i},k_{\nu_i}\right)\boldsymbol{a}_{\mathrm{T}}\left(l_{\tau_j},k_{\nu_j}\right)\right|$. $\left|\boldsymbol{a}_i^{\mathrm{H}}\boldsymbol{a}_j\right|$ can be expressed as (65)-(66), as shown at the top of this page. Let $\Delta l_\tau=l_{\tau_j}-l_{\tau_i}$, $\Delta k_\nu=k_{\nu_j}-k_{\nu_i}$, $\left|\boldsymbol{a}_i^{\mathrm{H}}\boldsymbol{a}_j\right|$ can be represented as

$$\left|\boldsymbol{a}_i^{\mathrm{H}}\boldsymbol{a}_j\right|=\frac{1}{N}\left|\sum_{\bar{n}=0}^{N-1}e^{\frac{-j2\pi}{N}\left\{[2Nc_1\Delta l_\tau-\Delta k_\nu]\bar{n}-Nd_{\bar{n},n_p}\left(\iota_{\tau_j}-\iota_{\tau_i}\right)\right\}}\right|$$

$$=\begin{cases}1, & \Delta l_\tau=0,\Delta k_\nu=0\\ \left|\sin c\left(\Delta k_\nu\right)\right|, & \Delta l_\tau=0,\Delta k_\nu\neq0\\ \frac{1}{N}\left|\sum_{\bar{n}=0}^{N-1}\eta_1\eta_2\right|, & \Delta l_\tau\neq0,\Delta k_\nu=0\\ \approx0, & \Delta l_\tau\neq0,\Delta k_\nu\neq0\end{cases}, \tag{67}$$

where $\eta_1=e^{\frac{-j2\pi}{N}2Nc_1\Delta l_\tau\bar{n}}$, $\eta_2=e^{j2\pi d_{\bar{n},n_p}\left(\iota_{\tau_j}-\iota_{\tau_i}\right)}$. Similar to the analysis in (22) and (23), when Δl_τ or Δk_ν is zero, (67) simplifies to a sinc function, peaking at $\Delta k_\nu=0$ or $\Delta l_\tau=0$, respectively. Therefore, when $\Delta l_\tau=\Delta k_\nu=0$ (i.e., $i=j$), the peak of $\left|\boldsymbol{a}_{\mathrm{T}}^{\mathrm{H}}\left(l_{\tau_i},k_{\nu_i}\right)\boldsymbol{a}_{\mathrm{T}}\left(l_{\tau_j},k_{\nu_j}\right)\right|$ is 1. As Δl_τ or Δk_ν increases, $\left|\boldsymbol{a}_{\mathrm{T}}^{\mathrm{H}}\left(l_{\tau_i},k_{\nu_i}\right)\boldsymbol{a}_{\mathrm{T}}\left(l_{\tau_j},k_{\nu_j}\right)\right|$ is close to zero. This can also be seen in Fig. 14. Therefore, for any $i\neq j$, $\left|\boldsymbol{a}_{\mathrm{T}}^{\mathrm{H}}\left(l_{\tau_i},k_{\nu_i}\right)\boldsymbol{a}_{\mathrm{T}}\left(l_{\tau_j},k_{\nu_j}\right)\right|$ generally satisfies

$$\left|\boldsymbol{a}_{\mathrm{T}}^{\mathrm{H}}\left(l_{\tau_i},k_{\nu_i}\right)\boldsymbol{a}_{\mathrm{T}}\left(l_{\tau_j},k_{\nu_j}\right)\right|\ll1. \tag{68}$$

Therefore, this proof is completed.

Appendix C
Proof of Theorem 3

The proof of Theorem 3 can be seen in (69)-(70). substituting $\boldsymbol{y}_T=\sum_{j=1}^{P}x_ph_i\boldsymbol{a}_{\mathrm{T}}\left(l_{\tau_j},k_{\nu_j}\right)$ and considering the orthogonality of $\boldsymbol{a}_{\mathrm{T}}\left(l_{\tau_i},k_{\nu_i}\right)$, (69) is obtained. From (67), with $\Delta l_\tau=l_{\tau_i}-\hat{l}_{\tau_i}\approx0$ and $\bar{k}_{\nu_i}\approx\hat{\bar{k}}_{\nu_i}$, we obtain (70). In addition, $\kappa_\nu-\kappa_{\nu_i}\in[-1,1]$. Therefore, $\left|\boldsymbol{a}_{\mathrm{T}}^{\mathrm{H}}\left(\hat{\bar{l}}_{\tau_i}+\hat{\iota}_{\tau_i},\hat{\bar{k}}_{\nu_i}+\kappa_\nu\right)\boldsymbol{y}_T\right|^2$ is a bounded unimodal function, with its extremum achieved at $\kappa_\nu=\kappa_{\nu_i}$. Therefore, this proof is completed.

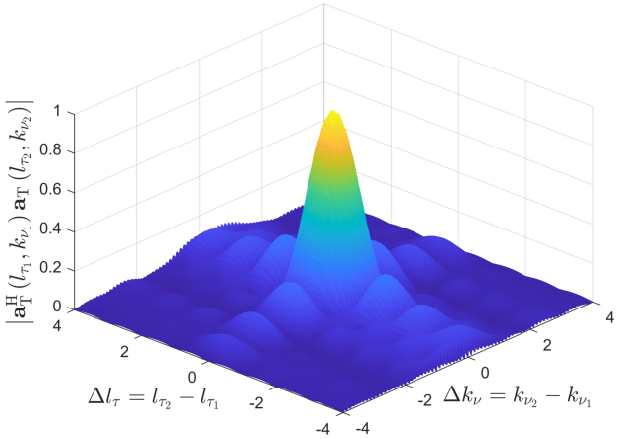

Fig. 14: Amplitude of $\left|\boldsymbol{a}_{\mathrm{T}}^{\mathrm{H}}\left(l_{\tau_i},k_{\nu_i}\right)\boldsymbol{a}_{\mathrm{T}}\left(l_{\tau_j},k_{\nu_j}\right)\right|$.

$$\left|\boldsymbol{a}_{\mathrm{T}}^{\mathrm{H}}\left(\hat{\bar{l}}_{\tau_i}+\hat{\iota}_{\tau_i},\hat{\bar{k}}_{\nu_i}+\kappa_\nu\right)\boldsymbol{y}_T\right|^2$$

$$\approx\left|x_ph_i\boldsymbol{a}_{\mathrm{T}}^{\mathrm{H}}\left(\hat{\iota}_{\tau_i},\hat{\bar{k}}_{\nu_i}+\kappa_\nu\right)\boldsymbol{a}_{\mathrm{T}}\left(l_{\tau_i},k_{\nu_i}\right)\right| \tag{69}$$

$$\approx\left|x_ph_i\right|\operatorname{sinc}\left(\kappa_\nu-\kappa_{\nu_i}\right). \tag{70}$$

References

[1] T. Wang, J. G. Proakis, and E. Masry *et al.*, "Performance degradation of OFDM systems due to Doppler spreading," *IEEE Trans. Wireless Commun.*, vol. 5, no. 6, pp. 1422–1432, Jun. 2006.

[2] L. Rugini and P. Banelli, "BER of OFDM systems impaired by carrier frequency offset in multipath fading channels," *IEEE Trans. Wireless Commun.*, vol. 4, no. 5, pp. 2279–2288, Sep. 2005.

[3] M. Noor-A-Rahim, Z. Liu, *et al*., "6G for vehicle-to-everything (V2X) communications: Enabling technologies, challenges, and opportunities," *Proceedings of the IEEE*, vol. 110, no. 6, pp. 712-734, Jun. 2022.

[4] R. Hadani *et al*., "Orthogonal time frequency space modulation," *2017 IEEE WCNC*, San Diego, CA, USA, pp. 1–6, Mar. 2017.

[5] Z. Wei *et al*., "Orthogonal time-frequency space modulation: a promising next-generation waveform," *IEEE Wireless Commun.*, vol. 28, no. 4, pp. 136–144, Aug. 2021.

[6] P. Raviteja *et al*., "Interference cancellation and iterative detection for orthogonal time frequency space modulation," *IEEE Trans. Wireless Commun.*, vol. 17, no. 10, pp. 6501–6515, Oct. 2018.

[7] S. Li, J. Yuan, and W. Yuan, *et al*., "Performance analysis of coded OTFS systems over high-mobility channels," *IEEE Trans. Wireless Commun.*, vol. 20, no. 9, pp. 6033-6048, Sept. 2021.

[8] P. Raviteja, K. T. Phan, and Y. Hong, "Embedded pilot-aided channel estimation for OTFS in delay–Doppler channels," *IEEE Trans. Veh. Technol.*, vol. 68, no. 5, pp. 4906-4917, May 2019.

[9] Z. Wei, W. Yuan, and S. Li, *et al*., "Off-grid channel estimation with sparse Bayesian learning for OTFS systems," *IEEE Trans. Wireless Commun.*, vol. 21, no. 9, pp. 7407–7426, Sep. 2022.

[10] Q. Wang, Y. Liang, Z. Zhang, and P. Fan, "2D off-grid decomposition and SBL combination for OTFS channel estimation," *IEEE Trans. Wireless Commun.*, vol. 22, no. 5, pp. 3084–3098, May 2023.

[11] X. Li, P. Fan, Q. Wang, and Z. Liu, "Grid evolution for doubly fractional channel estimation in OTFS systems," *IEEE Trans. Veh. Technol.* (Early Access), pp. 1–5, 2024.

[12] S. Gopalam, I. B. Collings, and S. V. Hanly *et al*., "Zak-OTFS implementation via time and frequency windowing," *IEEE Trans. Commun.*, vol. 72, no. 7, pp. 3873-3889, July 2024.

[13] F. Lampel, A. Avarado and F. M. J. Willems, "On OTFS using the discrete Zak transform," 2022 IEEE International Conference on Communications Workshops, Seoul, Korea, Republic of, pp. 729-734, 2022.

[14] A. Bemani, N. Ksairi, and M. Kountouris, "AFDM: a full diversity next generation waveform for high mobility communications," *2021 ICC Workshops*, Jun. 2021, pp. 1–6.

[15] A. Bemani, G. Cuozzo, N. Ksairi, and M. Kountouris, "Affine frequency division multiplexing for next-generation wireless networks," *2021 17th ISWCS*, Sep. 2021, pp. 1–6.

[16] A. Bemani, N. Ksairi, and M. Kountouris, "Affine frequency division multiplexing for next generation wireless communications," *IEEE Trans. Wireless Commun.*, vol. 22, no. 11, pp. 8214–8229, Nov. 2023.

[17] H. Yin, Y. Tang, and A. Bemani *et al*., "Affine frequency division multiplexing: Extending OFDM for scenario-flexibility and resilience," *IEEE Wireless Commun.*, vol. 32, no. 6, pp. 200-208, Dec. 2025.

[18] Z. Sui *et al*., "Multi-functional chirp signalling for next-generation multi-carrier wireless networks: communications, sensing and ISAC perspectives," arXiv:2508.06022, 2025.

[19] H. S. Rou, K. R. R. Ranasinghe, and V. Savaux *et al*., "Affine frequency division multiplexing (AFDM) for 6G: properties, features, and challenges," *IEEE Communications Standards Magazine* (Early Access), Jan. 2026.

[20] Q. Li, J. Li, and M. Wen *et al*., "Affine frequency division multiplexing for 6G networks: fundamentals, opportunities, and challenges," *IEEE Netw.*, vol. 40, no. 1, pp. 88-97, Jan. 2026.

[21] A. Bemani, "Affine frequency division multiplexing (AFDM) for wireless communications," Sorbonne Universite, France, Tech. Rep. ´ NNT:2023SORUS610, 2023.

[22] T. Erseghe, N. Laurenti and V. Cellini, "A multicarrier architecture based upon the affine Fourier transform," *IEEE Trans. Commun.*, vol. 53, no. 5, pp. 853-862, May 2005.

[23] X. Ouyang and J. Zhao, "Orthogonal chirp division multiplexing," *IEEE Trans. Commun.*, vol. 64, no. 9, pp. 3946–3957, Sep. 2016.

[24] E. Başar, Ü. Aygölü, E. Panayırcı, and H. V. Poor, "Orthogonal frequency division multiplexing with index modulation," *IEEE Trans. Signal Process.* , vol. 61, no. 22, pp. 5536–5549, Nov. 2013.

[25] Y. Tao, M. Wen, Y. Ge, and J. Li, "Affine frequency division multiplexing with index modulation," *2024 IEEE WCNC*, Apr. 2024, pp. 1–6.

[26] J. Zhu, Q. Luo, and G. Chen *et al*., "Design and performance analysis of index modulation empowered AFDM system," *IEEE Wireless Commun. Lett.*, vol. 13, no. 3, pp. 686–690, Mar. 2024.

[27] G. Liu, T. Mao, R. Liu, and Z. Xiao, "Pre-chirp-domain index modulation for affine frequency division multiplexing," *2024 IWCMC*, Ayia Napa, Cyprus, May, 2024, pp. 0473-0478.

[28] H. S. Rou, K. Yukiyoshi, and T. Mikuriya *et al*., "AFDM chirp-permutation-index modulation with quantum-accelerated codebook design," *58th Asilomar Conference on Signals, Systems, and Computers*, May 2024.

[29] H. S. Rou, G. T. F. de Abreu, "Chirp-permuted AFDM: a new degree of freedom for next-generation versatile waveform design," arXiv:2507.20825,2025.

[30] H. Yuan *et al*., "PAPR Reduction with pre-chirp selection for affine frequency division multiplexing," *IEEE Wireless Commun. Lett.*, vol. 14, no. 3, pp. 736-740, March 2025.

[31] Z. Sui, Z. Liu, and L. Musavian *et al*., "Generalized spatial modulation aided affine frequency division multiplexing," Jan. 2025, [online]: https://arxiv.org/abs/2501.10865.

[32] Y. Ni, Z. Wang, P. Yuan, and Q. Huang, "An AFDM-based integrated sensing and communications," *2022 International Symposium on Wireless Communication Systems*, Hangzhou, China: IEEE, Oct. 2022, pp. 1–6.

[33] A. Bemani, N. Ksairi, and M. Kountouris, "Integrated sensing and communications with affine frequency division multiplexing," *IEEE Wireless Commun. Lett.*, vol. 13, no. 5, pp. 1255–1259, May 2024.

[34] J. Zhu, Y. Tang, and F. Liu *et al*., "AFDM-based bistatic integrated sensing and communication in static scatterer environments," *IEEE Wireless Commun. Lett.*, vol. 13, no. 8, pp. 2245–2249, Aug. 2024.

[35] H.Yin, Y.Tang, and Y.Ni *et al*., "Ambiguity function analysis of AFDM signals for integrated sensing and communications". *IEEE J. Sel. Areas Commun.*, 2025.

[36] Q. Luo, P. Xiao, and Z. Liu *et al*., "AFDM-SCMA: A promising waveform for massive connectivity over high mobility channels," IEEE Trans. Wireless Commun., vol. 23, no. 10, pp. 14421-14436, Oct. 2024.

[37] H. Yin and Y. Tang, "Pilot aided channel estimation for AFDM in doubly dispersive channels," *2022 ICCC*, Aug. 2022, pp. 308–313.

[38] W. Benzine, A. Bemani, N. Ksairi, and D. Slock, "Affine frequency division multiplexing for compressed sensing of time-varying channels," *2024 IEEE 25th SPAWC Workshop*, Sep. 2024, pp. 916–920.

[39] W. Benzine, A. Bemani, N. Ksairi, and D. Slock, "Affine frequency division multiplexing for communications on sparse time-varying channels," *GLOBECOM 2023*, Dec. 2023, pp. 4921–4926.

[40] F. Yang, S. Luo, and L. Wu *et al*., "An AFDM off-grid channel estimation based on sparse Bayesian learning," *IEEE 24th ICCT*, Chengdu, China, 2024, pp. 1565-1569.

[41] H. Yin, X. Wei, Y. Tang, and K. Yang, "Diagonally reconstructed channel estimation for MIMO-AFDM with inter-Doppler interference in doubly selective channels," *IEEE Trans. Wireless Commun.* (Early Access), 2024.

[42] M. Avriel and D. J. Wilde, "Optimality proof for the symmetric Fibonacci search technique," *The Fibonacci Quarterly*, vol. 4, no. 3, pp. 265–269, Oct. 1966.

[43] M. Subasi *et al*., "An improvement on Fibonacci search method in optimization theory," *Applied Mathematics and Computation*, vol. 147, no. 3, pp. 893–901, Jan. 2004.

[44] C. Y. Chong *et al*., "Generalized Fibonacci search method in one-dimensional unconstrained non-linear optimization," *Pertanika Journal of Science and Technology*, vol. 29, no. 2, Apr. 2021.

[45] I. A. Khan, S. K. Mohammed, "Low complexity channel estimation for OTFS modulation with fractional delay and Doppler", arXiv:2111.06009, 2021.